OPTIMIZATION OF COUPLING FROM A SUB-WAVELENGTH METAL NANOAPERTURE TO A GAUSSIAN MODE

by

MUTHIAH ANNAMALAI

Presented to the Faculty of the Graduate School of

The University of Texas at Arlington in Partial Fulfillment

of the Requirements

for the Degree of

MASTER OF SCIENCE IN ELECTRICAL ENGINEERING

THE UNIVERSITY OF TEXAS AT ARLINGTON

August 2007

ACKNOWLEDGEMENTS

I thank prof. Vasilyev for the privilege to be a part of his Nonlinear Optics and Nanophotonics research group, to work on 10-Gb/s optical communication system, and later the nanoaperture computation. I also thank prof. Vasilyev for showing me the rigor and discipline in doing science, and his patience in advising me and accomodating me for almost 2 years now.

I thank Prof. Weidong Zhou, Dr. Nikolai Stelmakh and Prof. Jung-Chih Chiao for being on the thesis committee.

I thank my family and friends for their continued support and wisdom. I would like thank my mother Kamala, father Annamalai, and my uncle Ranganathan for providing me with this wonderful opportunity to go to graduate school. I would also like to thank Valli & Nathan for support, hospitality and friendship during these two years in Dallas.

I also thank Pallavi Patki and Sarath Chandra Samudrala, for the suggestions during work in Nonlinear Optics and Nanophotonics lab.

July 23, 2007

ABSTRACT

OPTIMIZATION OF COUPLING FROM A SUB-WAVELENGTH METAL NANOAPERTURE TO A GAUSSIAN MODE

Publication No. _____

MUTHIAH ANNAMALAI, M.S.

The University of Texas at Arlington, 2007

Supervising Professor: Michael Vasilyev

We model the surface resonance effects in a 1D-array of corrugations on a metal-dielectric film with a sub-wavelength nanoaperture, following the earlier work by Moreno *et al* [1]. We are interested in computing the coupling of the highly-directional light field emerging from the metal nanoaperture to the lowest-order Gaussian mode. We follow the approach by Vasilyev *et al* [2], to compute the coupling to the fundamental Gaussian mode.

We have developed an optimization routine to compute the field emission patterns from a metal nanoaperture and transmission coupling to the fundamental Gaussian mode for various geometrical parameters of the metal nanoastructure. We optimize for maximum T (power transmittance to the lowest-order mode) and T/L (ratio of transmittance to loss to higher-order modes), assuming zero absorption so that all reflected light can be potentially recycled in metal nanocavity.

This optimization work on the geometrical parameters of the cavity can be useful in fabricating a high Q cavity with desired resonant wavelength for the future construction of a high-efficiency single-photon emitter.

TABLE OF CONTENTS

LIST OF FIGURES

LIST OF TABLES

CHAPTER 1

INTRODUCTION

In 2002, a counter-intuitive phenomenon of narrow-beam emission from a subwavelength nanoaperture surrounded by corrugations (this structure is shown in Fig. 1.1) was experimentally reported [3]. The field of subwavelength optics has been traditionally neglected because of the difficulty imposed by low transmittance and large diffraction losses in such geometries. The new beam-narrowing phenomenon promises the convenient interface between subwavelength optics and propagating optical modes.

The P-polarization (TM) nature of the beam-narrowing effect is attributed to the presence of plasmonic surface resonance at the metal-dielectric interface. The field enhancement and highly-directional emission follow from the coupling of the surface waves to the free-space propagating modes due to momentum and energy conservation rules [1, 3, 4]. Surface waves are well known in metals and are referred to as surface plasmon polaritons, or plasmons, for short. Surface plasmons are present at a metal-dielectric interface, as bound electromagnetic modes when excited by P-polarized (TM) waves, as discussed in Appendix A. As has been shown in [1], the surface modes appear even in *perfect* metal structures, provided that they have corrugations. This will be the case analyzed in this thesis.

Simply put, subwavelength optics allows creation of photonic systems beyond the diffraction limit, offering field enhancements of more than order of magnitude and the advantages of nanometer scale. The advances in this research area are expected to provide new design tools in subwavelength optics regime for applications such as optical data storage [5], nonlinear optics, single-photon emitters for quantum communication

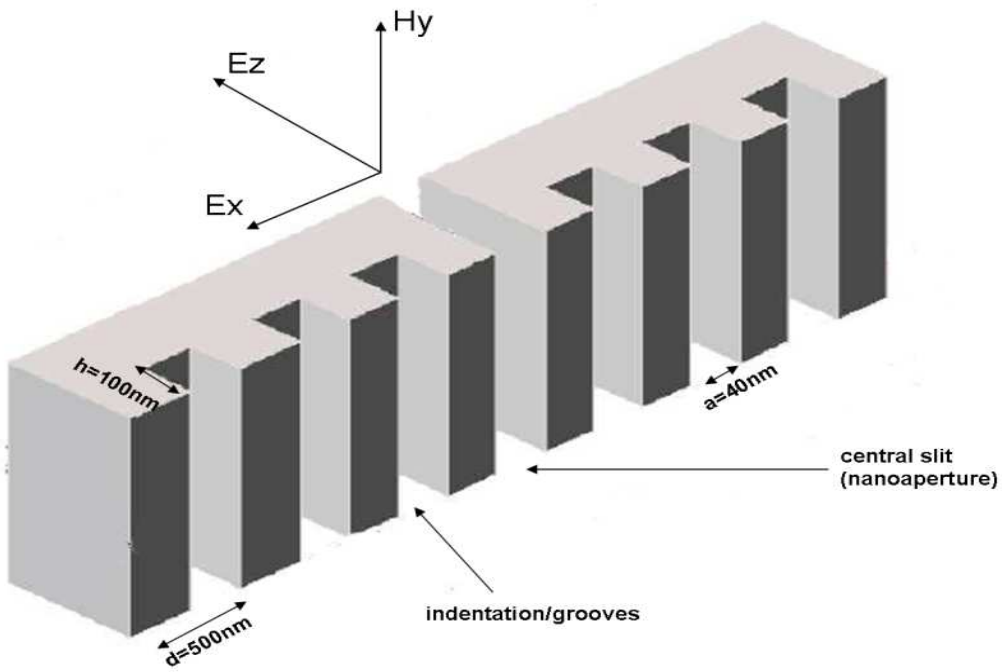

Figure 1.1. A schematic of the metal nanoaperture surrounded by periodic corrugations.

and linear-optics-based quantum computing [2], sensors based on Surface Enhanced Raman Spectroscopy (SERS), etc. These exciting applications are enabled by the e-beam lithography and focused-ion-beam writing technologies available for patterning and working with metals and semiconductors at the nanometer scale [5].

The theoretical work on corrugated subwavelength metal nanostructures has provided several degrees of freedom for engineering applications. The geometrical parameters such as number, periodicity, and depth of the grooves for 1-D periodic arrays [1], and 2-D arrays with arbitrary hole shapes in place of corrugations [6], directly affect the resonant characteristics. Such design parameters give a method to select an optimal structure for the application at specific choice of field enhancement level, focusing distance, resonant wavelength, or coupling coefficients.

Initial work has created parameterized universal charts relating the resonant wavelength to the geometry [7]. In 2004, Pendry and co-workers [8] resolved the origin of the field enhancement effect observed in non-resonant and resonant mode excitations of the surface plasmons. They explained the field enhancements in the non-resonant case due to pseudo-plasmons generated in perfect conductors, and also showed the degrees of freedom available for design of surface plasmon devices including waveguides.

Our interest is to use these subwavelength structures to build single-photon emitters, with high ouput coupling efficiency to the fundamental Gaussian mode (TEM0). The emitter placed within the metal-slit nanocavity will produce deterministic single-photon emission enhanced by the Purcell effect [9]. In a standing-wave cavity, where the dipole emitter is located at the crest (antinode) of the electrical field and is aligned with its direction, the Purcell factor is written as

$$F = \frac{3\lambda^3}{2\pi^2}\frac{Q}{V}\ , \tag{1.1}$$

where Q is the cavity quality factor, V is the mode volume, and λ is the wavelength of light in the cavity.

We expect the single-photon emitter in the subwavelength nanocavity to yield efficiency of coupling to the Gaussian mode at least comparable to that reported by Yamamoto and co-workers [10], who used a micropost-cavity approach with coupling efficiency of $\approx 38\%$.

This thesis work directly applies the results from the modeling of emission from a subwavelength 1-D periodic metal nanostructure by Moreno *et al* [1, 4], to the coupling of light from that subwavelength structure to a Gaussian mode. This extends upon previous work of Vasilyev *et al* [2] by searching wide parameter space for various geometries that give a high overall transmission coupling factor for use in a single-photon emitter.

The rest of this thesis is organized as follows. In Chapter 2, we re-derive the equations of the subwavelength metal-nanoaperture model following Moreno [1] and using scalar diffraction theory from the first principles. From the resulting set of linear equations, the magnetic field emerging from the metal nanoaperture is obtained. We also discuss the coupling to the fundamental Gaussian mode, from Vasilyev *et al* [2], and use it as the metric for our search.

Careful optimization of computing integrals involved in the model of subwavelength metal nanoaperture has been carried out in [11], and the results are reported in Chapter 3. Specifically, simplifying integrals involving special functions to avoid singularities, and ordering of the parametric searches to reduce computation and reuse certain parts of results, are explained.

The specific parametric search solver algorithms are detailed in Chapter 4. We also show how our solver can accurately replicate published results from Ref. [1], and use this as a measure of confidence in our simulation results. In this thesis work, we report searches to find geometries with optimum transmission coupling factors. The specific search spaces and details are reported in Chapter 4.

The results of our searches for transmission coupling coefficient T and transmission to loss ratio T/L are presented in Chapter 5. We present graphs and specific numerical results and discuss the general trend of parameters involved in this search and how they affect the metrics T and T/L.

We summarize the results of the thesis and discuss future work in Chapter 6.

CHAPTER 2
DIFFRACTED FIELD FROM A SUBWAVELENGTH SLIT

We present the derivation of the diffracted fields from the subwavelength metal nanoaperture from first principles, reproducing the results of Moreno *et al* [1]. To do that, we employ scalar diffraction theory for a TM-polarized incident wave. Then, we apply the results of the derivation to analyze coupling to the fundamental Gaussian mode. Figure 2.1 below illustrates the 2D structure we analyze in this thesis.

2.1 Problem definition

We are interested in computing the diffracted fields excited by a TEM wave propagating in a subwavelength metal slit (nanoaperture), which is surrounded by periodic corrugations (grooves). We also calculate the coupling factors from the diffracted fields to the lowest-order (fundamental) Gaussian mode. Finally, we want to find the optimum geometries that give the highest coupling factors to this mode.

We are specifically concerned with the particular 2D geometry of periodic grooves (corrugations) made in a metal-dielectric interface with a subwavelength slit, shown in Figs. 2.1 and 2.2. The field enhancement phenomenon is due to the surface-wave resonance effect observed only in case of illumination by TM-waves.

We seek to derive expressions for the coupling to the lowest-order (fundamental) Gaussian mode as a way to optimize metal-nanoaperture devices for operation with other Gaussian-beam optical elements for various purposes mentioned in Chapter 1.

We treat both the transmission and reflection properties of the subwavelength metal nanoaperture corresponding to Fig. 2.2.

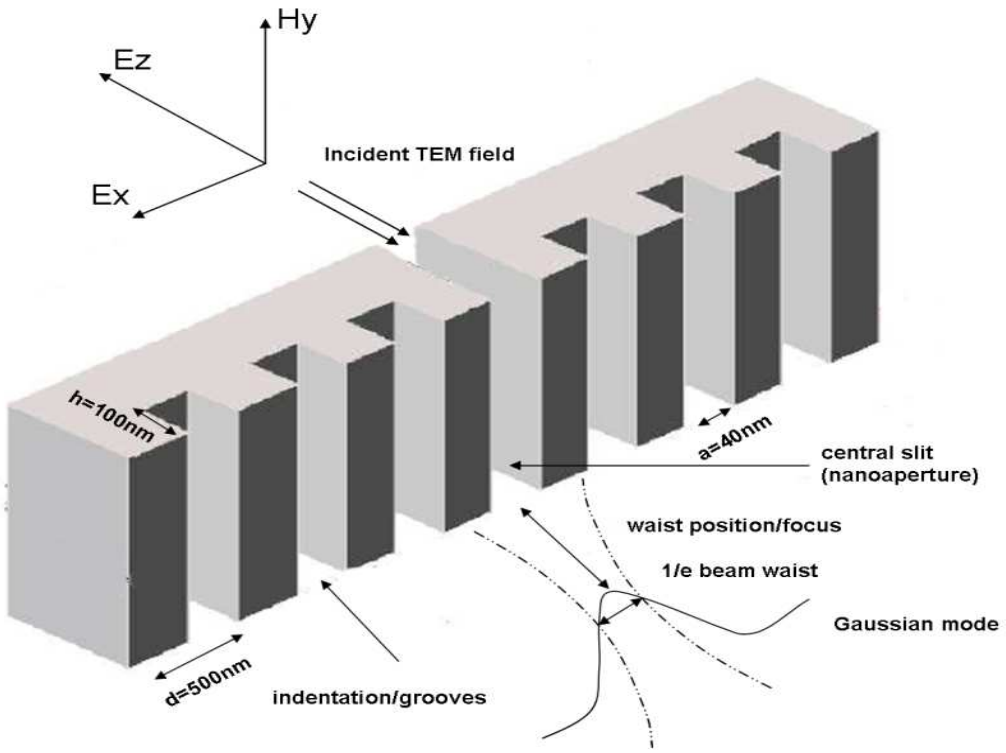

Figure 2.1. Coupling light to the fundamental Gaussian mode from the subwavelength metal nanoaperture.

2.2 2D TM Waves

2D electromagnetic problems (i.e. ones in which no variation in y-dimension occurs) can be analyzed by decomposing the fields over TE ($E_x = E_z = H_y = 0$) and TM ($H_x = H_z = E_y = 0$) subsets [12]. TM (P-polarization) excitation is required for the geometry of Fig. 2.2 in order to observe surface field enhancement.

Maxwell's equations are given by

$$\nabla \times \mathcal{H} = \epsilon_0 \frac{\partial \mathcal{E}}{\partial t} , \tag{2.1}$$

$$\nabla \times \mathcal{E} = -\mu_0 \frac{\partial \mathcal{H}}{\partial t} . \tag{2.2}$$

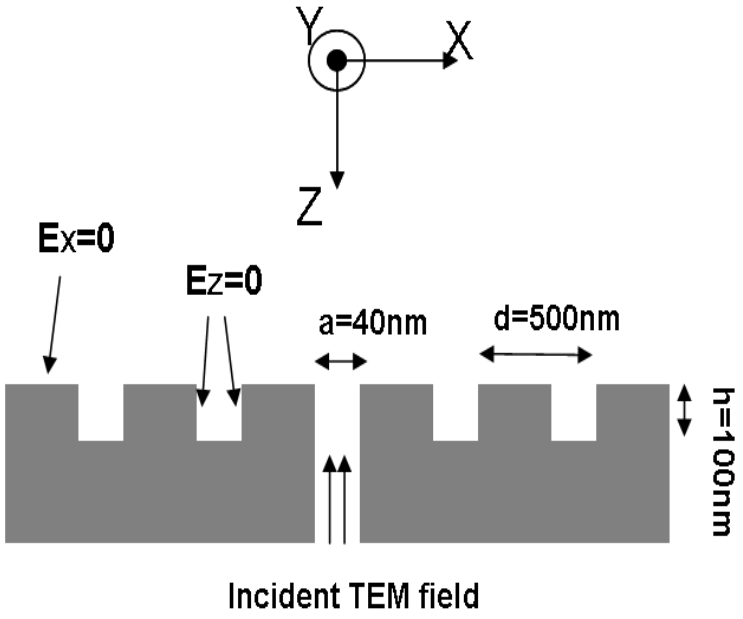

Figure 2.2. TM wave around metal nanoaperture.

For time-harmonic fields $\mathcal{H} = \mathbf{H}e^{-i\omega t}$, $\mathcal{E} = \mathbf{E}e^{-i\omega t}$, and these equations become

$$\nabla \times \mathbf{H} = -ikc\epsilon_0\mathbf{E} \,, \tag{2.3}$$

$$\nabla \times \mathbf{E} = ikc\mu_0\mathbf{H} \,, \tag{2.4}$$

where $k = \omega/c$. Note that all the results that follow can be extended to the case of a specific dielectric by replacing ϵ_0 by $\epsilon\epsilon_0$ everywhere.

For TM fields, H-field is a scalar (because $H_x = H_z = 0$), which makes it suitable for scalar diffraction theory analysis. (For TE fields same holds for E-field, thus any 2D problem can be treated as 2 scalar diffraction problems in TM and TE [12].) For TM field and geometry of Figs. 2.1 and 2.2, we have $H_x = H_z = E_y = 0$, with remaining components H_y, E_x and E_z that are functions of x and z (no dependence on y).

Maxwell's curl equations for the TM-case in component form are:

$$ikc\mu_o H_y = \frac{\partial E_x}{\partial z} - \frac{\partial E_z}{\partial x} , \tag{2.5}$$

$$-ikc\epsilon_0 E_x = -\frac{\partial H_y}{\partial z} . \tag{2.6}$$

It is easy to see that $\psi(x,z) = E_x$, E_z, or H_y satisfies the Helmholtz equation $(\nabla^2+k^2)\psi = 0$. In Sections 2.4 and 2.5, we will set the boundary conditions on the electric field $E_x\,(z=0)$ and compute the scattered field $H_y\,(\vec{r})$ as a function of the boundary values using scalar diffraction theory, with a proper choice of Green's function.

2.3 TEM mode of a metal slab waveguide

Let us begin with describing the lowest-order mode of the waveguide formed by a free-space slab between two perfectly conducting metal plates, as shown in Fig. 2.3. If we consider the electric and magnetic fields in the slab, i.e. $\mathcal{E}(\vec{r},t) = \hat{x}E_x(\vec{r})e^{-i\omega t} = \hat{x}E_x(x,y)e^{-i(\omega t \pm kz)}$ and $\mathcal{H}(\vec{r},t) = \hat{y}H_y(\vec{r})e^{-i\omega t} = \hat{y}H_y(x,y)e^{-i(\omega t \pm kz)}$, then the lowest-order mode is TEM, for which

$$\begin{aligned} H_y &= \sqrt{\frac{\epsilon_o}{\mu_o}}E_x , \quad \text{for wave travelling in } +z \text{ direction,} \\ H_y &= -\sqrt{\frac{\epsilon_o}{\mu_o}}E_x , \quad \text{for wave travelling in } -z \text{ direction,} \end{aligned} \tag{2.7}$$

and $E_x(x,y) = const$, i.e. there is no field variation in x-direction [13]. Here, $\hat{x}$, $\hat{y}$ are the unit vectors in the x- and y-directions. Quantity

$$\eta = \frac{E_x}{H_y} = \sqrt{\frac{\mu_o}{\epsilon_o}} = 377\Omega \tag{2.8}$$

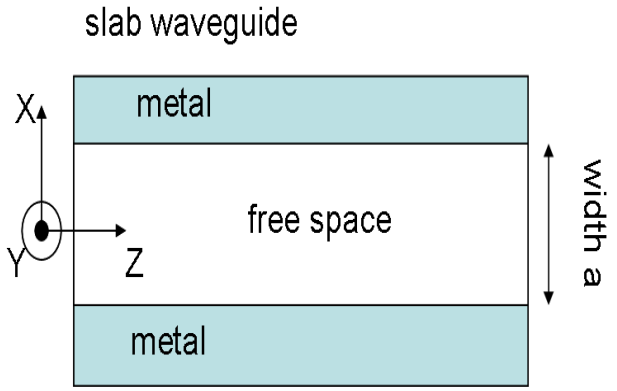

Figure 2.3. TEM wave in a metal slab waveguide.

is referred to as "impedance of vacuum." Conditions $H_z = E_z = E_y = H_x = 0$ hold inside our slab waveguide. Since both H_z and E_z components along the propagation direction z are zero, this mode is called the transverse electromagnetic, or TEM, wave. It is useful to note that TEM wave does not have a cut-off. The next-order modes, TM_1 and TE_1, both have cutoffs at $\lambda_c = 2a$, i.e do not propagate in slabs that are narrower than $\lambda/2$.

Now let us assume that at $z = 0$,

$$E_x(\vec{r}) = E_0 \ , \tag{2.9}$$

and that the waveguide is short-circuited at $z = h$, where

$$E_x(\vec{r}) = 0 \ . \tag{2.10}$$

In that case, the electric field is given by

$$E_x(\vec{r}) = E_1 e^{-ikz} + E_2 e^{ikz}, \tag{2.11}$$

i.e it consists of two waves counter-propagating in the slab. At $z = h$, the field evaluates to

$$E_1 e^{-ikh} + E_2 e^{ikh} = 0 \ , \tag{2.12}$$

and we have

$$E_1 = -E_2 e^{2ikh}. \tag{2.13}$$

From this, we have at $z = 0$:

$$E_x(\vec{r}) = E_2 \left(1 - e^{2ikh}\right) = E_0 \ , \tag{2.14}$$

i.e.

$$E_2 = \frac{E_0}{1 - e^{2ikh}} \ . \tag{2.15}$$

The corresponding magnetic field

$$\begin{aligned} H_y(\vec{r}) &= -\frac{E_1}{\eta} e^{-ikz} + \frac{E_2}{\eta} e^{ikz} \\ &= \frac{E_2}{\eta} \left[e^{ik(2h-z)} + e^{ikz}\right]. \end{aligned} \tag{2.16}$$

At $z = h$

$$H_y(\vec{r}) = \frac{2E_2}{\eta} \, e^{ikh}, \tag{2.17}$$

and at $z = 0$

$$H_y(\vec{r}) = \frac{E_2}{\eta}\left[1 + e^{2ikh}\right] = \frac{E_0}{\eta}\frac{1 + e^{2ikh}}{1 - e^{2ikh}} = i\frac{E_x(\vec{r})}{\eta\tan(kh)} \ . \tag{2.18}$$

In other words, the impedance at $z = 0$ is

$$Z = \frac{E_x}{H_y} = -i\eta\tan(kh) \ . \tag{2.19}$$

In Section 2.5, we will also need to analyze the situation where slab is excited by a $-z$-travelling wave with E_x-field magnitude $A_0/\sqrt{a}$. At $z = 0$, the slab is open-ended, producing a reflected wave with amplitude $(E_0 - A_0)/\sqrt{a}$, where $E_0/\sqrt{a}$ is E_x-field magnitude at $z = 0$, and the factor $\sqrt{a}$ is the normalization by the slab width. H_y-field at $z = 0$ is, therefore,

$$\begin{aligned} H_y &= -\frac{A_0}{\eta\sqrt{a}} + \frac{E_0 - A_0}{\eta\sqrt{a}} \\ &= \frac{1}{\eta\sqrt{a}}\left(E_0 - 2A_0\right) \ . \end{aligned} \tag{2.20}$$

2.4 Scalar diffraction theory for a planar screen

We treat the problem of diffraction from the corrugated metal-nanoaperture using scalar diffraction theory.

By the second Green's theorem we have

$$\int\int_A (G\nabla^2 H_y - H_y\nabla^2 G)\mathrm{d}A = \oint_C \left(G\frac{\partial H_y}{\partial n} - H_y\frac{\partial G}{\partial n}\right)\mathrm{d}C, \tag{2.21}$$

where $\partial/\partial n$ is a partial derivative in the outward normal direction at each point of the curve C surrounding area A.

If the scalar field H_y represents the amplitude of a harmonic light wave, then it satisfies the Helmholtz equation $(\nabla^2 + k^2)H_y = 0$. From this, Kirchhoff-Helmholtz integral theorem can be obtained with a proper choice of G, called the Green's function [14], defined as the solution of $(\nabla^2 + k^2)G = \delta(\vec{r} - \vec{r}\,')$.

The integral theorem of Kirchhoff-Helmholtz finds the field at a point P_0 in space as a function of the field and its derivative on a closed curve (for 2D theorem) surrounding that point. Goodman [14] only gives the Kirchhoff-Helmholtz formula for the 3D problem, thus we need to derive the 2D formula for this theorem.

Since for Green's theorem to work, both $G(\vec{r}, \vec{r}\,')$ and $H_y(\vec{r})$ have to have continuous 0th, 1st and 2nd derivatives, area A should exclude point P_0 with coordinate $\vec{r}\,' = \vec{r}$. To do that, we surround point P_0 with infinitesimally small circle C_ϵ of radius ϵ, so that area A is contained between C and C_ϵ (see Fig. 2.4). Then, within A, left-hand side of Eq. (2.21) is zero, and

$$\oint_{C+C_\epsilon} \left(G\frac{\partial H_y}{\partial n} - H_y\frac{\partial G}{\partial n} \right) = 0 \ . \tag{2.22}$$

We are interested in using Eq.(2.22) for diffraction on a planar screen at $z = 0$, as in Fig 2.4. In what follows, we will show that $H_y(\vec{r})$ in point P_0 depends on H_y and $\partial H_y/\partial z$ along the screen. Therefore, to eliminate $\partial H_y/\partial z$ (or H_y) from that equation, it makes sense to choose $G(\vec{r}, \vec{r}\,')$ whose value (or value of its normal derivative, respectively) vanishes on the screen. We choose the latter option (i.e. $\partial G/\partial n = \partial G/\partial z' = 0$ at $z = 0$) by using the following 2D Green's function:

$$G(\vec{r}, \vec{r}\,') = H_0^{(1)}(k|\vec{r} - \vec{r}\,'|) + H_0^{(1)}(k|\vec{r}^{\,*} - \vec{r}\,'|) \ , \tag{2.23}$$

where

$$\begin{aligned} \vec{r}^{\,*} &= x\hat{x} - z\hat{z} \ , \\ \vec{r} &= x\hat{x} + z\hat{z} \ . \end{aligned} \tag{2.24}$$

In these equations $H_0^{(1)}$ is a Hankel function describing cylindrical wave from a 2D point source P_0, and $\vec{r}^{\,*}$ is a coordinate of a point P_0^*, mirror image of P_0 with respect to the screen. Equation (2.23) describes two harmonic oscillators in phase with each other, yielding field continuity across the screen face, with normal derivative being zero. (Note that, to eliminate $\partial H_y/\partial z$ by setting $G = 0$ at $z' = 0$ instead, we would have needed to subtract the two Hankel functions in Eq. (2.23).) At the screen ($z' = 0$), $|\vec{r} - \vec{r}\,'| = |\vec{r}^{\,*} - \vec{r}\,'|$, therefore

$$\begin{aligned} \frac{\partial G}{\partial n} &= \frac{\partial G}{\partial z'} \\ &= \left[kH_0^{(1)\prime}(k|\vec{r} - \vec{r}\,'|)\frac{z' - z}{|\vec{r} - \vec{r}\,'|} + kH_0^{(1)\prime}(k|\vec{r}^{\,*} - \vec{r}\,'|)\frac{z' + z}{|\vec{r}^{\,*} - \vec{r}\,'|} \right]_{z'=0} = 0 \ , \end{aligned} \tag{2.25}$$

where $H_0^{(1)\prime}$ denotes the derivative of the Hankel function with respect to its argument. The Green's function on the plane of the screen ($z' = 0$) is

$$G(\vec{r}, \vec{r}\,') = 2H_0^{(1)}(k|\vec{r} - x'\hat{x}|) \ . \tag{2.26}$$

Let us now evaluate

$$\oint_{C_\epsilon} \left(G\frac{\partial H_y}{\partial n} - H_y\frac{\partial G}{\partial n} \right) \mathrm{d}C_\epsilon \ . \tag{2.27}$$

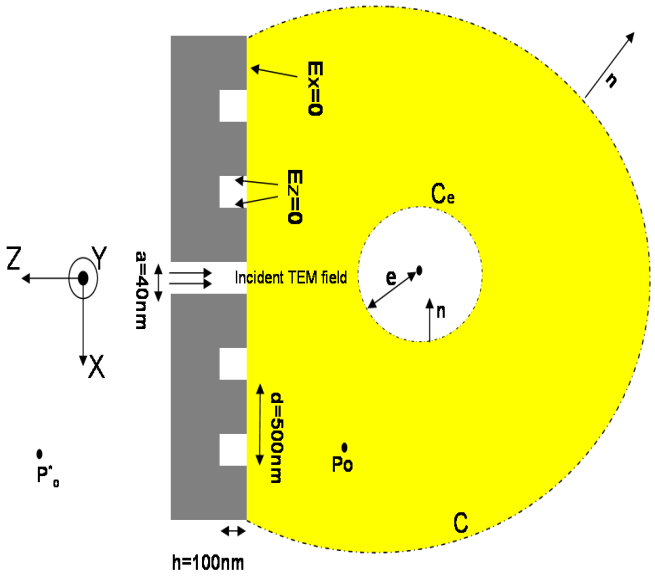

Figure 2.4. Planar diffraction treated by scalar diffraction theory.

The first term after integration will be proportional to[1]

$$2\pi\epsilon H_0^{(1)}(k\epsilon) \approx i4\epsilon \ln(\epsilon) \ , \tag{2.28}$$

whose limit is 0 for $\epsilon \rightarrow 0$. At the same time, the second term after integration becomes

$$H_y(\vec{r})2\pi\epsilon\frac{\partial H_0^{(1)}(k\epsilon)}{\partial\epsilon} = H_y(\vec{r})2\pi\epsilon\frac{2i}{\pi\epsilon} = 4iH_y(\vec{r}) \ . \tag{2.29}$$

The integral over curve C includes integration over the screen ($z' = 0$) and integration over the semi-circle of radius $R \rightarrow \infty$. Assuming that we only deal with outgoing waves on that semi-circle, H_y decreases at least as fast as a diverging cylindrical wave, making

[1]For $x \rightarrow 0$, Hankel function of zeroth order, first kind, has asymptotic $H_0^{(1)}(x) = 1 + i\frac{2}{\pi}\left[\ln x + \gamma - \ln z\right] + O(x^2) + iO(x^2 \ln x)$, where $\gamma = 0.57721566490153286061$.

the contribution of the semi-circle vanish at $R \to \infty$, which is the Sommerfeld radiation condition for 2D. Then,

$$\oint_{C+C_\epsilon} \left(G\frac{\partial H_y}{\partial n} - H_y\frac{\partial G}{\partial n} \right) \mathrm{d}C = 4iH_y(\vec{r}) + \left[\int_{-\infty}^{+\infty} G(\vec{r},\vec{r}\,')\frac{\partial H_y(\vec{r}\,')}{\partial z'}\,\mathrm{d}x' \right]_{z'=0}$$
$$= 4iH_y(\vec{r}) + 2ikc\epsilon_0 \int_{-\infty}^{+\infty} H_0^{(1)}(k|\vec{r} - x'x|)E_x(x')\mathrm{d}x', \quad (2.30)$$

where we used Eq. (2.6). Finally,

$$H_y(\vec{r}) = -\frac{k}{2\eta}\int_{-\infty}^{+\infty} H_0^{(1)}(k|\vec{r} - x'x|)E_x(x')\mathrm{d}x', \quad (2.31)$$

where $\eta = \sqrt{\mu_o/\epsilon_o} = 377\ \Omega$.

2.5 Diffraction from a periodically corrugated structure

In the structure of Fig 2.2, the slit and each groove can be considered metal slab waveguides supporting only the fundamental TEM mode. The incident TEM field is exiting from a corrrugated output face. Then, for the plane $z = 0$, we obtain from Eqs. (2.19), (2.20), and (2.31):

$$E_x(x) = \frac{ik}{2}\tan(kh)\int_{-\infty}^{+\infty} H_0^{(1)}(k|x - x'|)E_x(x')\,\mathrm{d}x' \quad \text{(for grooves)} \quad (2.32)$$

and

$$E_0 = 2A_0 - \frac{k\sqrt{a}}{2}\int_{-\infty}^{+\infty} H_0^{(1)}(k|x - x'|)E_x(x')\,\mathrm{d}x' \quad \text{(for slit)}, \quad (2.33)$$

where $E_x(x) = 0$ between the corrugations, and $E_x(x) = E_\alpha$ at the corrugation with index α (slit has index $\alpha = 0$). In other words,

$$E_x(x) = \sum_\alpha E_\alpha \phi_\alpha(x), \tag{2.34}$$

where

$$\phi_\alpha(x) = \begin{cases} \frac{1}{\sqrt{a}} & \text{for } x \in \text{groove } \alpha, \\ 0 & \text{elsewhere,} \end{cases} \tag{2.35}$$

and

$$\int_{-\infty}^{+\infty} \phi_\alpha^*(x)\phi_\beta(x)\mathrm{d}x = \delta_{\alpha\beta} \tag{2.36}$$

for $\alpha, \beta \in [-N, N]$. By projecting Eqs. (2.32) and (2.33) onto $\phi_\alpha^*(x)$ and integrating over x, we obtain

$$\begin{aligned} &(2A_0 - E_0)\,\delta_{\alpha 0} - i\frac{E_{\alpha\neq 0}}{\tan(kh)} = \\ &\qquad \frac{k}{2}\sum_\beta E_\beta \int_{-\infty}^{+\infty}\int_{-\infty}^{+\infty} \phi_\alpha^*(x) H_0^{(1)}(k|x-x'|)\phi_\beta(x')\mathrm{d}x\mathrm{d}x'. \end{aligned} \tag{2.37}$$

By using the notation

$$G_{\alpha\beta} = \frac{ik}{2}\int_{-\infty}^{+\infty}\int_{-\infty}^{+\infty} \phi_\alpha^*(x) H_0^{(1)}(k|x-x'|)\phi_\beta(x')\mathrm{d}x\mathrm{d}x', \tag{2.38}$$

we rewrite conveniently the main equation as

$$(G_{\alpha\alpha} - \epsilon_\alpha)\,E_\alpha + \sum_{\beta\neq\alpha} G_{\alpha\beta}E_\beta = 2iA_0\delta_{\alpha 0}, \tag{2.39}$$

where ϵ_α is defined as

$$\epsilon_\alpha = \begin{cases} -i & , \quad \alpha = 0, \\ \frac{1}{\tan(kh)} & , \quad \alpha \neq 0. \end{cases} \tag{2.40}$$

From this, we can write the total transmittance as

$$T_{\text{total}} = \frac{|A_0|^2 - |E_0 - A_0|^2}{|A_0|^2} = 1 - \left|\frac{E_0}{A_0} - 1\right|^2 = 1 - R \, , \tag{2.41}$$

where

$$R = |r|^2 = \left|\frac{E_0}{A_0} - 1\right|^2 \tag{2.42}$$

is the reflectance back into the slit waveguide, and

$$r = \frac{E_0}{A_0} - 1 \tag{2.43}$$

is the amplitude reflection coefficient.

The lowest-order (fundamental) 1D Gaussian mode TEM0 has the form

$$g(x,z) = \text{Gaussian}(x,z) = \frac{\exp\left\{-\frac{1}{2}\frac{kx^2}{\left[ka_0^2 - i(z-z_0)\right]}\right\}}{\sqrt[4]{\pi a_0^2\left[1 + (z-z_0)^2/(ka_0^2)^2\right]}} \, , \tag{2.44}$$

where a_0 is the beam waist size also called the $1/e$ intensity radius, and z_0 is the focal position where this beam waist occurs. We assume the mode to be propagating in the $-z$ direction (for $+z$, replace k by $-k$), and to be normalized to 1:

$$\int_{-\infty}^{+\infty} |g^*(x,z)|^2 dx = 1. \tag{2.45}$$

When considering coupling to the Gaussian mode TEM0, we write the coupling coefficient as the overlap integral, with power transmission T as follows:

$$t = -\eta \frac{\int_{-\infty}^{+\infty} g^*(x,0) H_y(x) \mathrm{d}x}{A_0}, \tag{2.46}$$

$$T = |t|^2 = \eta^2 \frac{\left| \int_{-\infty}^{+\infty} g^*(x,0) H_y(x) \mathrm{d}x \right|^2}{|A_0|^2}. \tag{2.47}$$

Note that $T + R + L = 1$, where L is the loss due to coupling to higher-order modes.

We also note that, for the case of the incident wave with no corrugations ($N = 0$), Equation (2.39) reduces to

$$E_0 = \frac{2iA_0}{G_{00} + i}, \tag{2.48}$$

$$E_{\alpha \neq 0} = 0, \tag{2.49}$$

so that

$$r = \frac{2i}{G_{00} + i} - 1, \tag{2.50}$$

$$T_{\text{total}} = 1 - |r|^2 = \frac{4\,\mathbf{Im}(G_{00})}{|G_{00} + i|^2}\,. \tag{2.51}$$

In the limiting case of $ka \ll 1$, we have $G_{00} \approx -\frac{ka}{\pi} \ln(ka) + i\frac{ka}{2}$, and $T_{\text{total}} \approx 2ka$.

2.6 Solutions

The solution to the integral equation can be written as a matrix equation, where we need to solve for E_α (the fields at the faces of the grooves) from Eq. (2.39), where α, β indices

are running from $-N$ to $+N$ through 0. This is a system of $2N+1$ linear equations with $2N+1$ variables E_α. It can be written in matrix formulation as

$$\mathbf{G'E_x} = \mathbf{E_{in}}, \tag{2.52}$$

where $G'_{\alpha\beta} = G_{\alpha\beta}$ for $\alpha \neq \beta$, and $G'_{\alpha\alpha} = G_{\alpha\alpha} - \epsilon_\alpha$, i.e.

$$\begin{bmatrix} G_{-N,-N}-\epsilon_{-N} & \dots & G_{-N,r} & G_{-N,+N} \\ \vdots & \dots & G_{-(N-1),r} & \vdots \\ G_{k,-N} & \ddots & \ddots & G_{k,N} \\ \vdots & \dots & G_{s,s}-\epsilon_s & \vdots \\ G_{N,-N} & \dots & G_{N,r} & G_{N,N}-\epsilon_N \end{bmatrix} \begin{bmatrix} E_{-N} \\ \vdots \\ E_{-r} \\ \vdots \\ E_N \end{bmatrix} = 2iA_o \begin{bmatrix} 0 \\ \vdots \\ \delta_{00} \\ \vdots \\ 0 \end{bmatrix}. \tag{2.53}$$

Equation (2.52) can be solved as

$$\mathbf{E_x} = \mathbf{G'^{-1}E_{in}} \ . \tag{2.54}$$

This system is solved for $\mathbf{E_x}$ using a computer inversion of $\mathbf{G'}$. Then, one can calculate the output emerging magnetic field as

$$H_y(\vec{r}) = -\frac{1}{\mu_0 c}\sum_\alpha E_\alpha G(\alpha, \vec{r}), \tag{2.55}$$

where

$$G(\alpha, \vec{r}) = \frac{k}{2}\int_{-\infty}^{+\infty} H_0^{(1)}(k|\vec{r} - x'\hat{x}|)\, \phi_\alpha^*(x')\, \mathrm{d}x'. \tag{2.56}$$

From the previous equations, one can calculate total transmittance T_{total} using Eq. (2.41), as well as the far-field intensity emission pattern $I(\theta)$ (to be discussed at the end of this Section).

Computationally, in order to calculate coupling to a Gaussian mode, one first needs to calculate $G_{\alpha\beta}$, then invert the matrix equation Eq.(2.53), and then compute the overlap integral T. Calculation of $G_{\alpha\beta}$ in x-domain requires taking a double integral. The same operation can be performed in the spatial frequency domain, where it is reduced to a single integral (convolution becomes product), but with a singularity inside:

$$G_{\alpha\beta} = \frac{i}{2\pi} \int_{-\infty}^{+\infty} \left[\frac{\sin(y/2)}{y/2} \right]^2 e^{iy\frac{d}{a}(\alpha-\beta)} \frac{\mathrm{d}y}{\sqrt{1-(y/\kappa)^2}} \ , \tag{2.57}$$

where

$$y = k_x a, \qquad \text{and} \quad \kappa = ka \ . \tag{2.58}$$

Using spatial-frequency-domain expression for normalized Gaussian,

$$\text{Gaussian}(k_x) = \sqrt[4]{4\pi a_0^2} \exp\left\{ -\frac{[ka_0^2 - i(z-z_0)]\, k_x^2}{2k} \right\} \ , \tag{2.59}$$

where the integral is normalized to 1, i.e.

$$\int_{-\infty}^{+\infty} |\text{Gaussian}(k_x)|^2 \, \frac{\mathrm{d}k}{2\pi} = 1, \tag{2.60}$$

we obtain

$$t = \frac{1}{2\pi A_0}\sqrt[4]{4\pi\frac{a_0^2}{a^2}}\sum_\alpha E_\alpha \int_{-\infty}^{+\infty}\frac{\sin(y/2)}{y/2}\frac{\exp\{-iy\frac{d}{a}\alpha - \frac{\kappa(a_0/a)^2+i[(z-z_0)/a]}{\kappa}\frac{y^2}{2}\}}{\sqrt{1-(y/\kappa)^2}}\,\mathrm{d}y. \quad (2.61)$$

The computational difficulty of the integrals Eqs. (2.57) and (2.61) is in their sensitivity to the step size near the singularity.

A more computationally attractive alternative in $G_{\alpha\beta}$ calculation is in reducing the double integral over x, x' to a single integral still in the x-domain (by simplifying it analytically), which is discussed in Section 3.1.

For Gaussian projection calculation, the most computationally efficient approach is to use far-field (i.e $r \to \infty$) asymptotic of $H_y(\vec{r})$. For $x \to \infty$, $H_0^{(1)}(x) \to \sqrt{\frac{2}{\pi x}}\, e^{i(x-\pi/4)}$. Assuming $x = r\sin\theta$, $z = -r\cos\theta$, we have

$$\begin{aligned} |\vec{r} - x'\hat{x}| = \sqrt{z^2+(x-x')^2} &= r\sqrt{\cos^2\theta + (\sin\theta - x'/2)^2} \\ &= r\sqrt{1 - 2\frac{x'}{r}\sin\theta + \left(\frac{x'}{r}\right)^2} \quad (2.62) \\ &\approx r - x'\sin\theta \quad \text{for } r\to\infty\,. \quad (2.63) \end{aligned}$$

Then, for $r \to \infty$,

$$\begin{aligned} H_y(\vec{r}) &\approx -\frac{k}{2\eta}\sqrt{\frac{2}{\pi k r}}\, e^{i(kr-\pi/4)}\int_{-\infty}^{+\infty} e^{-ik\sin\theta\, x'} E_x(x')\,\mathrm{d}x' \\ &= -\frac{1}{\eta}\sqrt{\frac{k}{2\pi r}}\, e^{i(kr-\pi/4)} E_x(k_x) \quad \text{for } k_x = k\sin\theta\,,\ \text{i.e. } |k_x| \le k\,. \quad (2.64) \end{aligned}$$

The spatial-frequency representation of the electric field on the face of the metal nanostructure is

$$E_x(k_x) = \int_{-\infty}^{+\infty} e^{-ik_x x} E_x(x) dx = \sum_\alpha E_\alpha \phi_\alpha(k_x)$$
$$= \sum_\alpha E_\alpha \sqrt{a} e^{-ik_x \alpha d} \left[\frac{\sin(k_x a/2)}{k_x a/2} \right] . \tag{2.65}$$

Using $k_x = k \sin\theta$, we can now re-write the overlap integral over the angle θ in far field as

$$t = \frac{\int_{-\frac{\pi}{2}}^{\frac{\pi}{2}} g^*(\theta) H_y^{\mathrm{Norm}}(\theta) \mathrm{d}\theta}{A_0} , \tag{2.66}$$

where we have omitted the constant phase factor $e^{-i[\Phi(r)+\pi/4]}$ with $\Phi(r) \approx -\frac{\pi}{2}$ being the Gouy phase shift for the Gaussian beam.

The transmittance T is given by

$$T = \frac{\left| \int_{-\frac{\pi}{2}}^{+\frac{\pi}{2}} g^*(\theta) H_y^{\mathrm{Norm}}(\theta) \right|^2}{|A_0|^2} . \tag{2.67}$$

In Eqs. (2.66) and (2.67), the Gaussian profile is

$$g(\theta) = \sqrt[4]{\frac{(ka_0)^2}{\pi}} e^{ikz_0 \cos\theta} e^{-(ka_0\theta)^2/2} , \tag{2.68}$$

with the sign convention such that $z_0 < 0$ is in front of the corrugated side, and

$$H_y^{\mathrm{Norm}}(\theta) = \sqrt{\frac{ka}{2\pi}} \frac{\sin[(ka\sin\theta)/2]}{(ka\sin\theta)/2} \sum_\alpha E_\alpha e^{-ikd\alpha\sin\theta} . \tag{2.69}$$

We note that

$$\int_{-\frac{\pi}{2}}^{\frac{\pi}{2}} |g(\theta)|^2 \, \mathrm{d}\theta = 1 \,, \tag{2.70}$$

and

$$\int_{-\frac{\pi}{2}}^{\frac{\pi}{2}} \left|H_y^{\mathrm{Norm}}(\theta)\right|^2 \mathrm{d}\theta = |A_0|^2 \, T_{\mathrm{total}} \ . \tag{2.71}$$

The last equation comes from the fact that far-field intensity emission pattern

$$I(\theta) = \frac{r \left|H_y(\vec{r})\right|^2 \eta}{|A_0|^2 \, T_{\mathrm{total}}/\eta} = \frac{ka}{2} \left[\frac{\sin(k_x a/2)}{k_x a/2}\right]^2 \frac{\left|\sum_\alpha E_\alpha e^{-ik_x \alpha d}\right|^2}{|A_0|^2 - |A_0 - E_0|^2} \,, \tag{2.72}$$

introduced in [1], is the ratio of the energy sent per unit angle θ in direction $\vec{r}$ to the total energy $|A_0|^2 T_{\mathrm{total}}/\eta$ emitted by the slit. $I(\theta)$ is normalized so that,

$$\int_{-\frac{\pi}{2}}^{\frac{\pi}{2}} I(\theta) \, \mathrm{d}\theta = 1 \,, \tag{2.73}$$

as one can easily see from the no-corrugations, $ka \ll 1$, case, where $|A_0|^2 T_{\mathrm{total}} = 2ka|A_0|^2$, $E_0 = -2A_0$, and $I(\theta) = \frac{1}{\pi}$ (uniform distribution). We see that

$$H_y^{\mathrm{Norm}}(\theta) = \lim_{r \to +\infty} \left[H_y(\vec{r})\sqrt{r}\eta\right] . \tag{2.74}$$

CHAPTER 3

OPTIMIZATION OF COMPUTATIONAL MODEL

The double integrals required to compute the problem are resolved into single integrals through clever use of substitution rules and properties of special functions, as reported in [11]. The details of the reductions are presented here.

We analytically integrate the Hankel function of the first kind and zero order $H_0^{(1)}(x)$ near zero using its asymptotic expansion. This process removes stepping on a singularity during integration and makes for a stable integral calculation.

3.1 Quasi-Green's function $G_{\alpha\beta}$ integral reduction

In what follows, the specific forms of the integrals are given, and 2D integrals are reduced to 1D by variable transformation. In certain places, the singularity of the Hankel function is eliminated by careful construction of the integral.

$$\begin{aligned} G_{\alpha\beta} &= \frac{ika}{2} \int_{\alpha\frac{d}{a}-\frac{1}{2}}^{\alpha\frac{d}{a}+\frac{1}{2}} \mathrm{d}y \int_{\beta\frac{d}{a}-\frac{1}{2}}^{\beta\frac{d}{a}+\frac{1}{2}} \mathrm{d}y' H_0^{(1)}(ka|y-y'|) \\ &= \frac{ika}{4} \int_{p'-1+|z-p|}^{p'+1-|z-p|} \mathrm{d}z' \int_{p-1}^{p+1} \mathrm{d}z\, H_0^{(1)}(ka|z|)\ , \end{aligned} \tag{3.1}$$

which yields

$$G_{\alpha\beta} = \frac{ika}{2} \int_{p-1}^{p+1} (1-|z-p|) H_0^{(1)}(ka|z|)\, \mathrm{d}z \tag{3.2}$$

with $p = (\alpha - \beta)\, d/a$. We have 2 cases,

1. $p = 0$, i.e. $\alpha = \beta$:

$$\begin{aligned} G_{00} &= \frac{ika}{2}\int_{-1}^{1}(1-|z|)H_0^{(1)}(ka|z|)\,\mathrm{d}z \\ &= ika\int_{0}^{1}(1-z)H_0^{(1)}(kaz)\,\mathrm{d}z \\ &= ika\int_{0}^{1}(1-z)[H_0^{(1)}(kaz) - \frac{2i}{\pi}\ln z + \frac{2i}{\pi}\ln z\,]\,\mathrm{d}z\,, \end{aligned} \tag{3.3}$$

which yields

$$G_{00} = ika\int_{0}^{1}(1-z)[H_0^{(1)}(kaz) - \frac{2i}{\pi}\ln z\,]\,\mathrm{d}z - \frac{3i}{2\pi}\,, \tag{3.4}$$

where function under the integral no longer has a singularity at $z = 0$.

2. $p \neq 0$, i.e. $\alpha \neq \beta$:

$$G_{\alpha\beta} = \frac{ika}{2}\int_{|p|-1}^{|p|}(1+z-|p|)H_0^{(1)}(kaz)\,\mathrm{d}z + \int_{|p|}^{|p|+1}(1-z+|p|)H_0^{(1)}(kaz)\,\mathrm{d}z\,, \tag{3.5}$$

where no singularities are present, since $|p| > 1$ for any $\alpha \neq \beta$.

3.2 Search order optimization

One useful optimization when carrying out search over large parameter spaces of various values of *N*, *d*, and *h*, is the symmetry of the quasi Green's function matrix $\mathbf{G}'$. When faced with solving $\mathbf{G}'\mathbf{E}_\mathbf{x} = \mathbf{E}_\mathrm{in}$, we only need to compute $\mathbf{G}$ for various *N, d*. We can simply reuse $\mathbf{G}$ for various depths *h*, because in matrix $\mathbf{G}'$ only the main diagonal elements change due to ϵ_α, so that $\mathbf{G}'$ is simply recalculated for each *h*.

Since profiling results on our code indicate that 90% of code execution time is spent on the calculation of elements in the quasi Green's matrix $\mathbf{G}$, we obtain significant speedup of the size of h-range (groove depth range) in large-scale parametric searches. This is directly useful in our thesis problem, when we search for optimizing coupling parameters over numerous geometries.

In calculating the Gaussian projection, we need to vary the waist position z_0 to obtain the maximum overlap. This is done after time-consuming calculation of the values of E_α, so it can be very fast.

CHAPTER 4

SOLVER FOR METAL-NANOAPERTURE MODEL

The simulation programs are written using numerical programming language Matlab (version 6, release 12). The solver is organized into a series of individual solver-functions and a set of driver routines that compute angular emission patterns, transmission coefficient, and coupling coefficient to Gaussian mode. In this chapter, the organization of the solver, description of the critical solver routines, validation of the solver routines, and specific steps in the parametric search and optimization are explained.

4.1 Organization

The solver is created to compute only the E, H fields at the output face of the 1D corrugated subwavelength metal-nanoaperture. To tackle this problem computationally, we need to solve the equations described in Chapters 2 and 3.

4.1.1 Algorithm for computing the diffracted fields

To compute the E, H fields at output face of a corrugated subwavelength metal nanoaperture, we complete the following steps:

1. Provide geometry details of the subwavelength structure. Typical values of the parameters are similar to values in Fig. 1.1.
    - N , number of grooves/indentations on either side of the central aperture
    - h , depth of the groove/indentation
    - a , central slit and groove width
    - d , periodicity of grooves

- λ , wavelength of the TM-field incident on nanoaperture.

2. Assume a normalized $\mathbf{E}_{\text{in}}$ incident electric field.
3. Compute the $\mathbf{G}$ matrix.
4. Solve for the electric field at slit face $\mathbf{E_x} = \mathbf{G'}^{-1}\mathbf{E_{in}}$.
5. Compute the far-field intensity pattern $I(\theta)$.
6. Compute normalized far-field magnetic field $H_y^{\text{Norm}}(\theta)$.

With these values, one has sufficient information to compute the coupling to a Gaussian mode.

4.1.2 Solver functions

Separate functions are created corresponding to each step of the algorithm. Such functions are listed below with their specific steps in the algorithm; a few other utility functions are also listed below for computing coupling and transmission factors.

1. *greens_quasi_2d*: computes the basic quasi greens matrix $\mathbf{G}$.
2. *greens_matrix*: corrects the greens matrix for ϵ_α factors in main diagonal, yielding $\mathbf{G'}$.
3. *efield_incident*: generates an E-field vector $\mathbf{E_{in}}$ incident only on the central slit.
4. *intensity_far_field*: computes the far-field intensity distribution $I(\theta)$ of the light emerging from the nanoaperture.
5. *couplingtx_slit2gaussian_atface*: compute the coupling to a 1D Gaussian mode TEM0, loss (coupling to higher-order modes), and the reflection factor.

4.2 Accuracy

The accuracy of the solver was verified as follows. For a numerical simulation, it is critical for us to ensure the results reported to be accurate, and reproducible. This section explains how we validated the solver, the benchmarks used and necessary parameters.

We have compared our results with [1] and with the transmission coupling values reported by Vasilyev *et al* [2]. We have ensured that the computation of the integrals, and special functions have a sufficient degree of accuracy.

4.2.1 Comparison with published literature

The first and most important validations of the solver come from matching comparisons to results in the published works of Moreno [1] and Vasilyev [2].

To compare with [1], we solved the nanoaperture geometry with $N = 10$, $a = 40$ nm, $d = 500$ nm, $h = 100$ nm used in [1] at resonant wavelength $\lambda = 560$ nm. The solver generated the cases described in graphs below, reproducing Figs. 2–4 in [1].

1. **Intensity emission patterns across the azimuthal plane**

   Intensity emission patterns $I(\theta)$ across the azimuthal angle θ for same geometry at 2 different wavelengths of $\lambda = 560$ nm, 800 nm, are shown in Figs. 4.1 left and right, respectively. Also the insets corresponding to the original paper are reproduced in Figs. 4.2 and 4.3. These figures show the relative enhancement in power at the output far-field. We compute data in Figs. 4.2 and 4.3 as Poynting vectors normalized to the no-corrugation geometry, $\frac{S(N=10,\theta)}{S(N=0,\theta)} = \frac{I(N=10,\theta)}{I(N=0,\theta)}$, to show enhancements in the field due to the presence of output corrugations.

2. **Azimuthal intensity emission patterns across wavelengths**

   The maps of intensity emission patterns $I(\theta)$ across the azimuthal angle θ in the wavelength range $\lambda = 400 - 1100$ nm for 3 different groove depths $h = 10$, 100, and 160 nm, given by Fig. 3 in [1], are reproduced exactly by our simulation, as shown in Figs. 4.4–4.6.

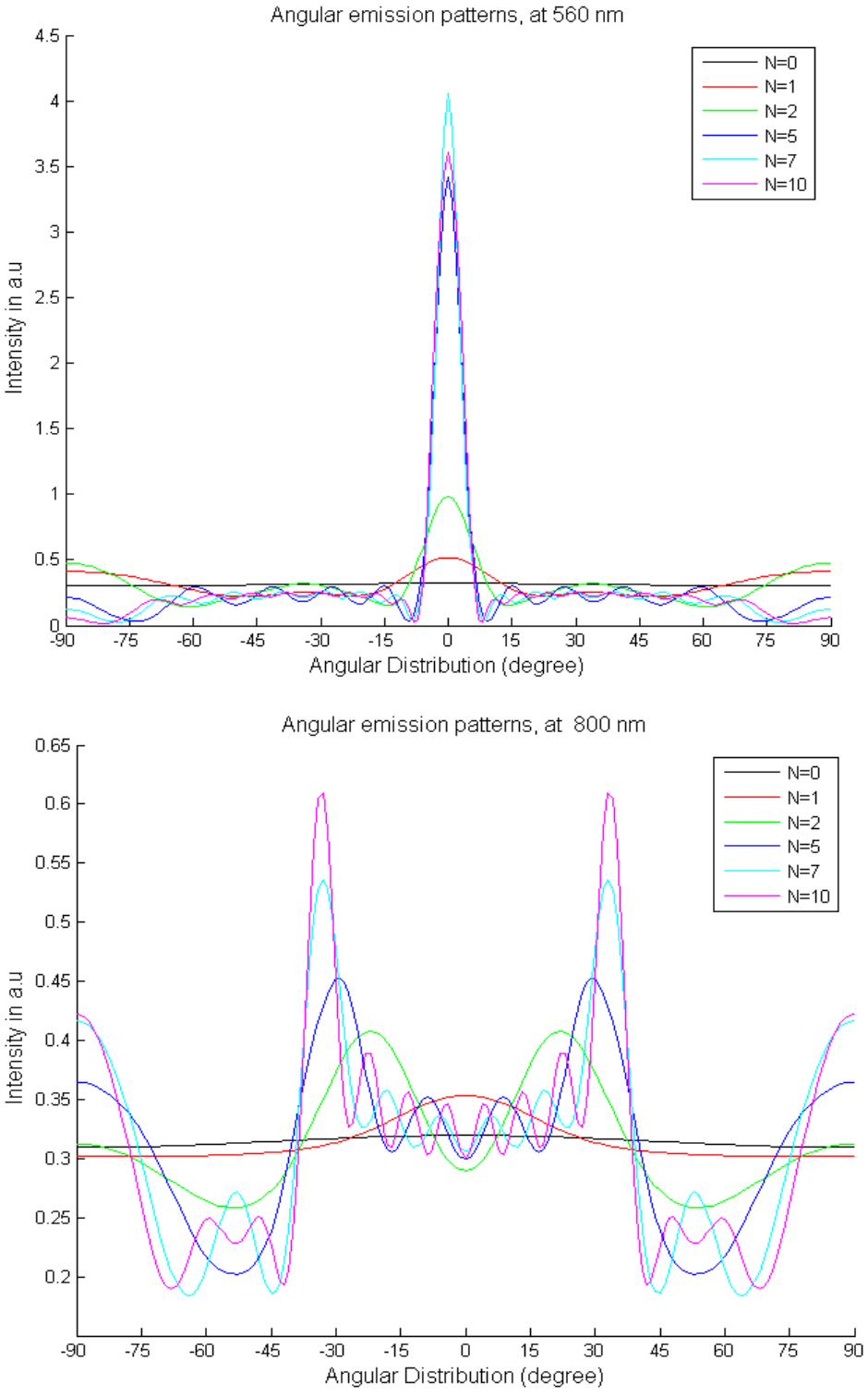

Figure 4.1. Intensity emission patterns $I(\theta)$ across the azimuthal angle θ at wavelengths (top) $\lambda = 560$ nm and (bot) $\lambda = 800$ nm for geometry N, h, d, $a = \{10,\ 100\text{ nm},\ 500\text{ nm},\ 40\text{ nm}\}$.

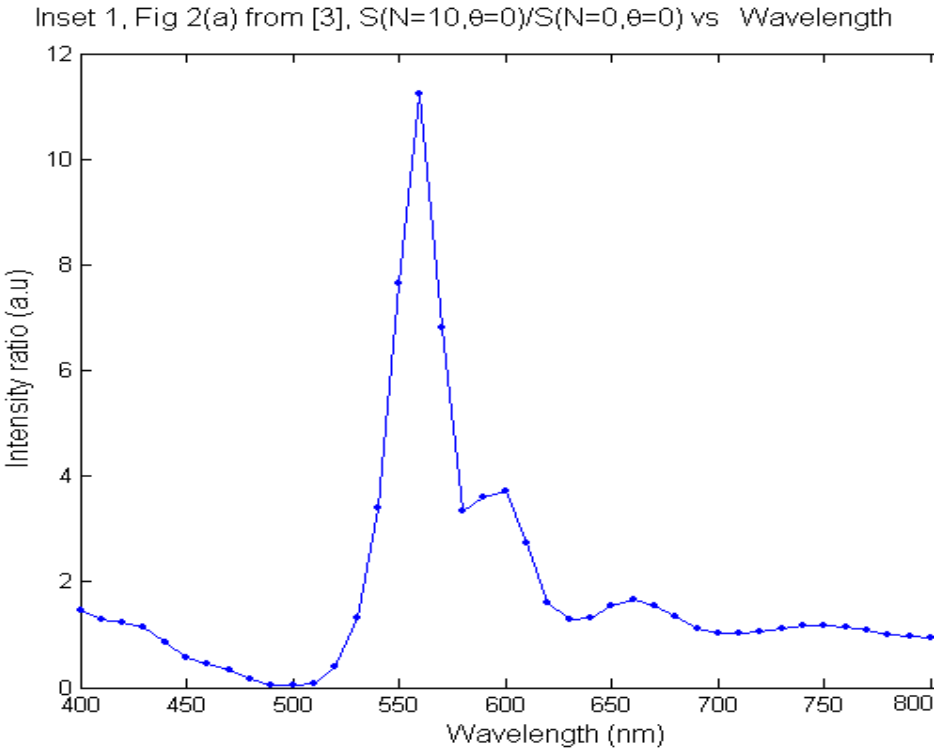

Figure 4.2. Relative enhancement in emission spectrum in wavelength range 400–800 nm due to corrugations, for geometry N, h, d, $a = \{10,\ 100\text{ nm},\ 500\text{ nm},\ 40\text{ nm}\}$.

3. **Normalized electric field across the slits**

   Figure 4.7 shows $|E_\alpha/E_0|$, i.e. electric field normalized to peak field, versus the groove number α for a fixed geometry and excitation at $\lambda = 560\text{ nm}, 800\text{ nm}$. This reproduces Fig. 4 of Moreno [1].

These graphs match exactly with the published figures of Moreno [1]. This is one important accuracy metric for a good confidence in the solver results.

The next check is comparison to the coupling coefficients reported by Vasilyev *et al* [2] for the geometry $N = 7$, $d = 500$ nm, $a = 40$ nm, $h = 100$ nm, $\lambda = 560$ nm. Coupling coefficients reported in the paper are: $T = |t_2|^2 = 30\%$ and $R = |r_2|^2 = 40\%$, $T/L \approx 1$ for a Gaussian mode (TEM0) with focus position $z_0 = 7\ \mu$m from the face of the film and beam waist size $a_0 = 1.4\ \mu$m. Our calculations also compare exactly with

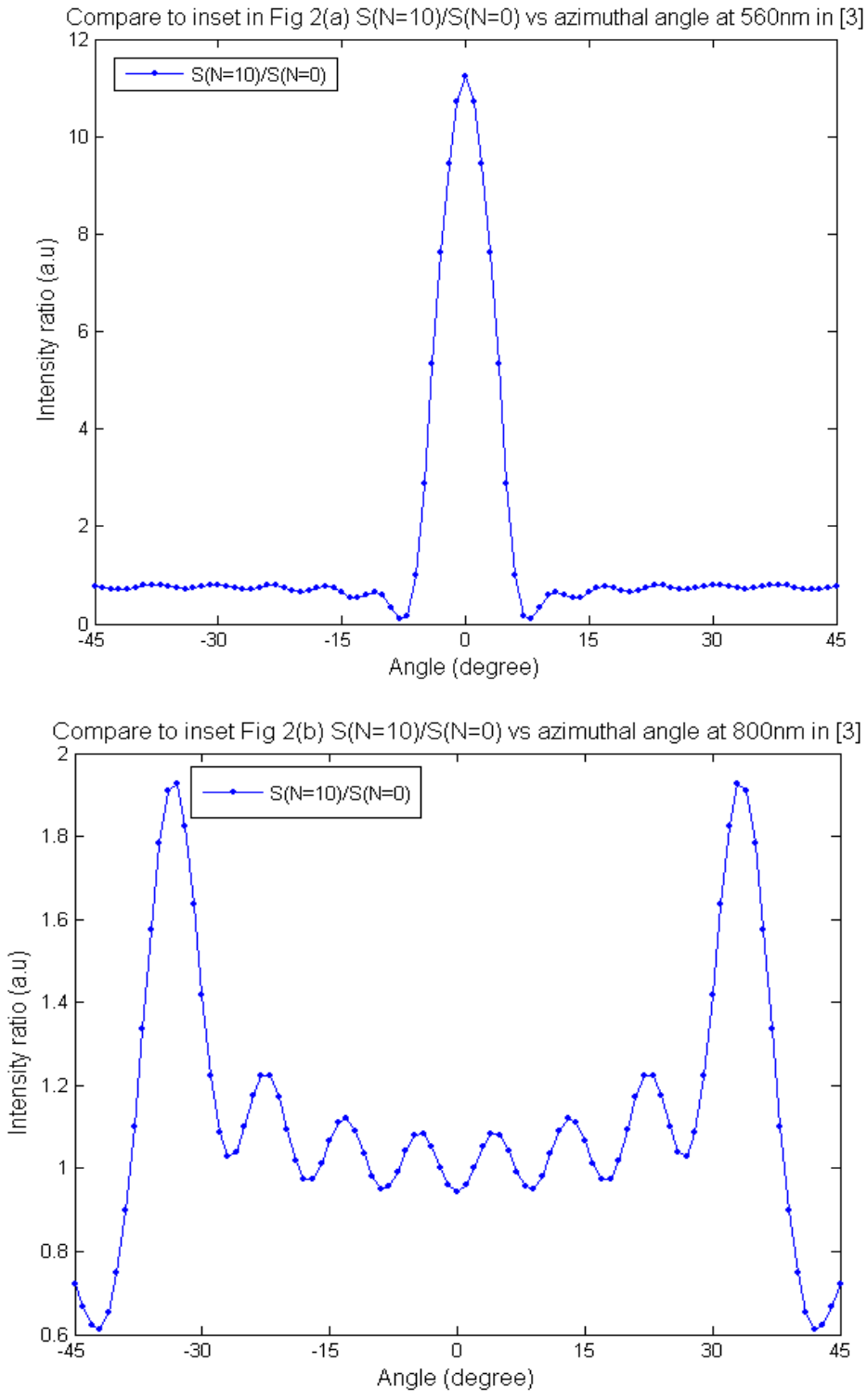

Figure 4.3. Relative enhancement in intensity emission pattern due to presence of corrugations, across azimuthal angle θ at (top) $\lambda = 560$ nm, (bottom) $\lambda = 800$ nm for geometry N, h, d, $a = \{10, 100\text{ nm}, 500\text{ nm}, 40\text{ nm}\}$.

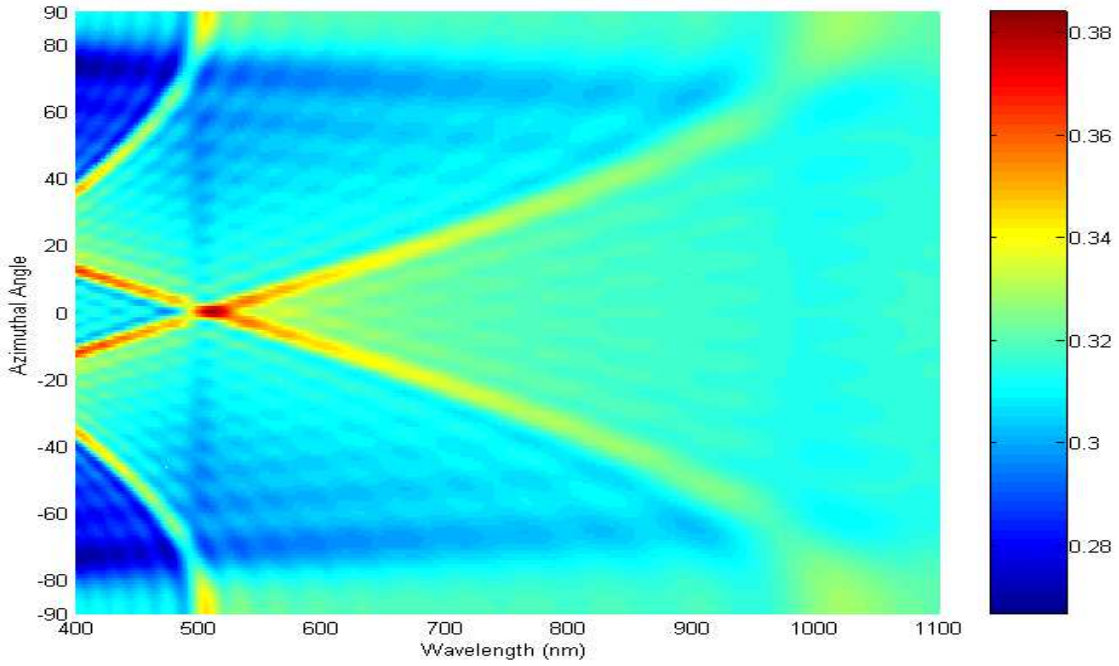

Figure 4.4. Azimuthal intensity emission patterns $I(\theta)$ for various wavelengths, for geometry N, h, d, $a = \{10, 10\text{ nm}, 500\text{ nm}, 40\text{ nm}\}$.

the reported transmission, reflection and transmission-to-loss ratio factors. This is the other important validation for the solver.

4.2.2 Numerical accuracy

Accuracy in computing special functions, and integrals contributes to the overall accuracy of the final transmission and coupling parameters. Careful optimization of the multiple integrals in Chapter 3 solves much of the problem, especially computing near singularities. Remaining computations are easily done using available routines, or well known algorithms. The Hankel function are built-ins of the Matlab numerical package used for simulations, and they consume the longest time in the calculation. We use trapezoid integration formulas, which require ≈ 50 points for integrals (3.4), (3.5) and ≤ 1000 points for calculating far field emission patterns and coupling to Gaussian mode.

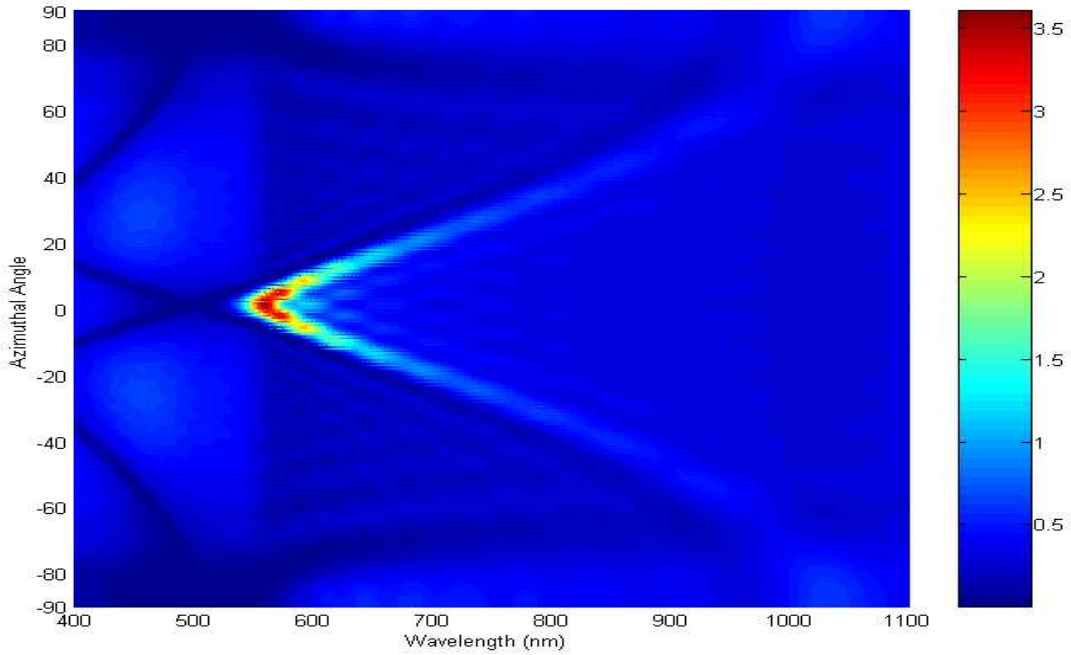

Figure 4.5. Azimuthal intensity emission patterns $I(\theta)$ for various wavelengths, for geometry N, h, d, $a = \{10, 100 \text{ nm}, 500 \text{ nm}, 40 \text{ nm}\}$. Observe the peak value of intensity around 3.5, which is $\approx$ 10 times the minimum, at $\lambda = 560$ nm.

4.3 Parametric search and optimization of transmission coupling

An important contribution of this thesis is the parametric search for a geometry and a Gaussian mode waist position that ensures a good coupling $T > 30\%$ to the Gaussian mode. This parametric search is the focus of the simulations in this thesis work. The parameters to be optimized for coupling to the Gaussian mode (TEM0) are the geometry of the structure, wavelength and waist position of the Gaussian mode.

We run a parametric search over the problem space given by groove number $N = [0 : 16]$, groove period $d = [200 : 50 : 1000]$ nm, groove depth $h = [10.1 : 2 : (\lambda/4 + 5)]$ nm, and wavelength $\lambda = [200 : 5 : 1000]$ nm. This translates into $17 \times 17 \times \sum_{\lambda=200,\,\text{step}\,5}^{1000} \text{length}\,[10.1 : 2 : (\lambda/4 + 5)] = 17 \times 17 \times 11743 =$ 3,393,727 cases of various geometries and wavelengths, for which we solve the problem.

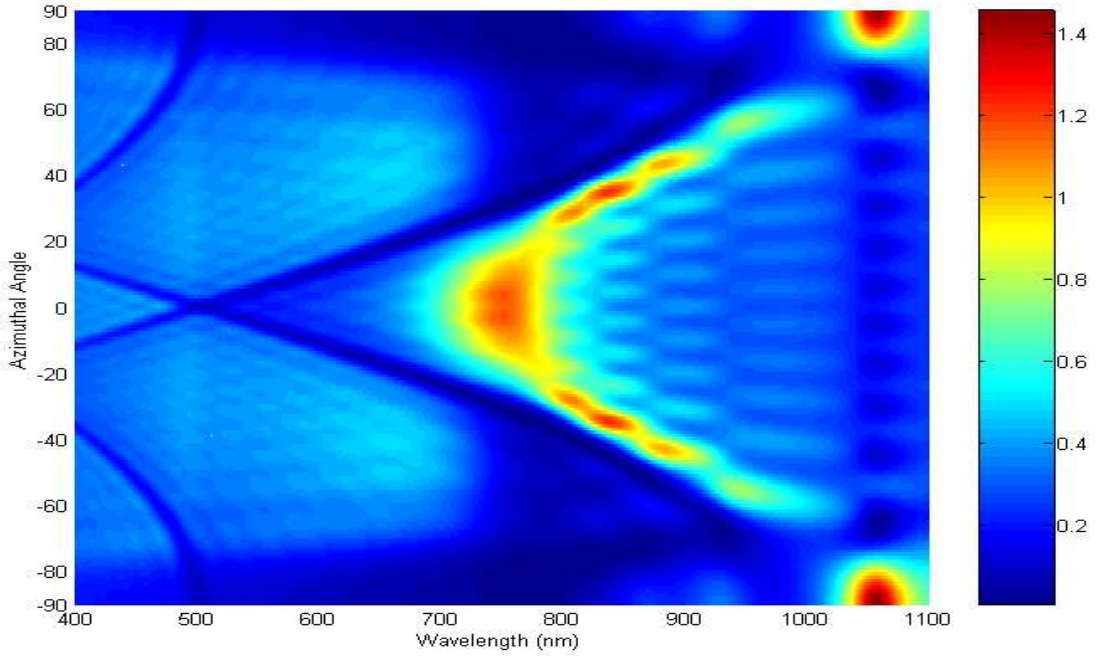

Figure 4.6. Azimuthal intensity emission patterns $I(\theta)$ for various wavelengths, for geometry N, h, d, $a = \{10, 160\text{ nm}, 500\text{ nm}, 40\text{ nm}\}$.

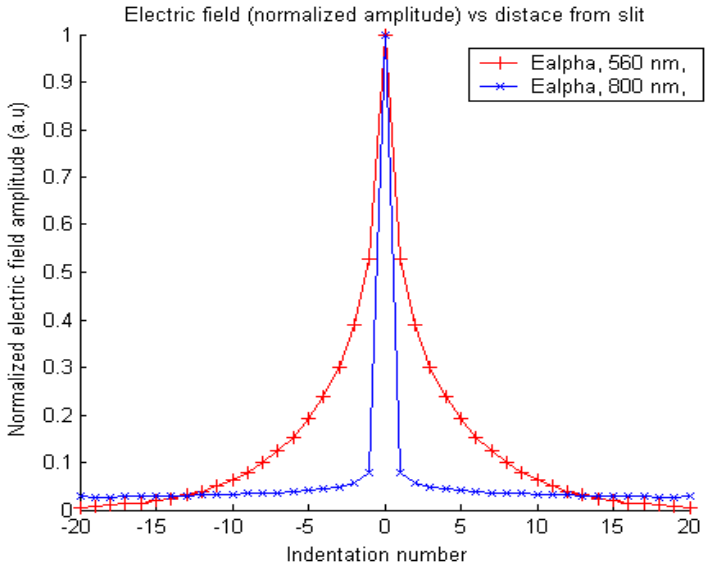

Figure 4.7. Relative field amplitudes $|E_\alpha/E_0|$ versus indentation number α at $\lambda = 560$ nm, $\lambda = 800$ nm for N, h, d, $a = \{20, 100\text{ nm}, 500\text{ nm}, 40\text{ nm}\}$.

The Gaussian mode coupling is computed in the post-processing stage, for the given scattered fields at the geometry and wavelength of TM-polarized light incident on it. Here we try to vary the waist position of the Gaussian beam over a specified range $-2ka_0^2 \cdots + 2ka_0^2$ with 161 steps, keeping the waist size at the minimum $\sim$ 1.4 μm achievable in a practical small-core single-mode fiber. The program searches for peak transmission coupling coefficients above 30% value reported by Vasilyev [2].

CHAPTER 5

RESULTS OF METAL-NANOAPERTURE SIMULATIONS

The running times of the programs increase in direct proportion to N, the number of corrugations in the geometry, as we solve for a $2N+1$ size matrix. The most time consuming part of the computation turns out to be filling the $\mathbf{G}'$ matrix, which is consequently due to computing the Hankel function. But the optimized solver takes very little time and can process all the geometries for the transmission coupling search within several hours on a standard PC.

Improving the T/L ratio is of interest when the subwavelength nanocavity is used as an open-ended waveguide resonator embedded with an active emitter, e.g. a quantum dot. Value of $T/L \approx 1$ was reported by Vasilyev [2]. Our optimization seeks to increase the value of this ratio. Under a perfect-metal assumption, all light reflected back at the nanoaperture-air interface is available for reuse in the nanocavity, i.e is not lost. So we only have to be concerned with Gaussian mode (TEM0) coupling, and reduce the losses to higher-order modes, which are irreversible. A large T/L ratio indicates that most of the light is coupled to the Gaussian mode of interest, rather than to the higher-order modes.

5.1 Optimization of T and T/L metrics with a fixed beam waist

In this round of simulations, we use the same Gaussian waist size $a_0 = 1.4$ μm for all wavelengths.

We report larger values of T/L up to 1.67 for a geometry with depth $h = 206$ nm, number of grooves $N = 4$, period $d = 800$ nm, slit width $a = 40$ nm, at wavelength

$\lambda = 1000$ nm coupled to a fundamental Gaussian mode with waist $a_0 = 1.4$ μm, and focus position $z_0 = 6773.27$ nm. For this geometry, $T = 0.22066$.

The peak transmission coupling of $T = 0.351$ was found for geometry with depth $h = 32.1$ nm, number of grooves $N = 16$, period $d = 250$ nm, slit width $a = 40$ nm, at wavelength $\lambda = 265$ nm when coupled to a fundamental Gaussian mode with same waist, but focus position optimized to $z_0 = 39501.1$ nm. For this geometry, $T/L = 0.84382$.

The summary of the searches is documented in Tables 5.1 and 5.2, and is also charted for convenience in Fig. 5.1. The general trend of the data shows an increase of the metrics with the number of grooves, saturating after $N \approx 3 \ldots 8$. The dependence of T and T/L metrics on wavelength λ and groove period d is also analyzed in Figs. 5.2 and 5.3, respectively.

These simulations were carried out with step in wavelength λ of 5 nm and step in period d of 50 nm. Thus, for a given wavelength, T or T/L can be maximized, primarily, by changing the period d. Since step in period is coarse compared to the step in wavelength, we see oscillations with period of 50 nm in Fig. 5.2, which indicate that, for some wavelengths (minima), the geometry is not optimum owing to an unsuitable d. Optimum d is typically less than $(0.8 - 0.9)\lambda$, which explains sharp roll-off at large d in Fig. 5.3, because the high end of d seems to be too large for given wavelength range.

The general observations from the simulations seem to suggest a trade-off between a larger T and a larger T/L, by the choice of geometry and wavelength. One can easily see that T is maximized at short-wavelength end, whereas T/L is maximized at the long-wavelength end of the range. A rapid increase in T/L with λ can be explained by the fact that the size of the beam waist a_0 in this run did not depend on λ. Thus, the angular spread of the long-wavelength Gaussian beams was wider, thereby capturing larger portion of the emitted light. In order to model the realistic scenario where far-field

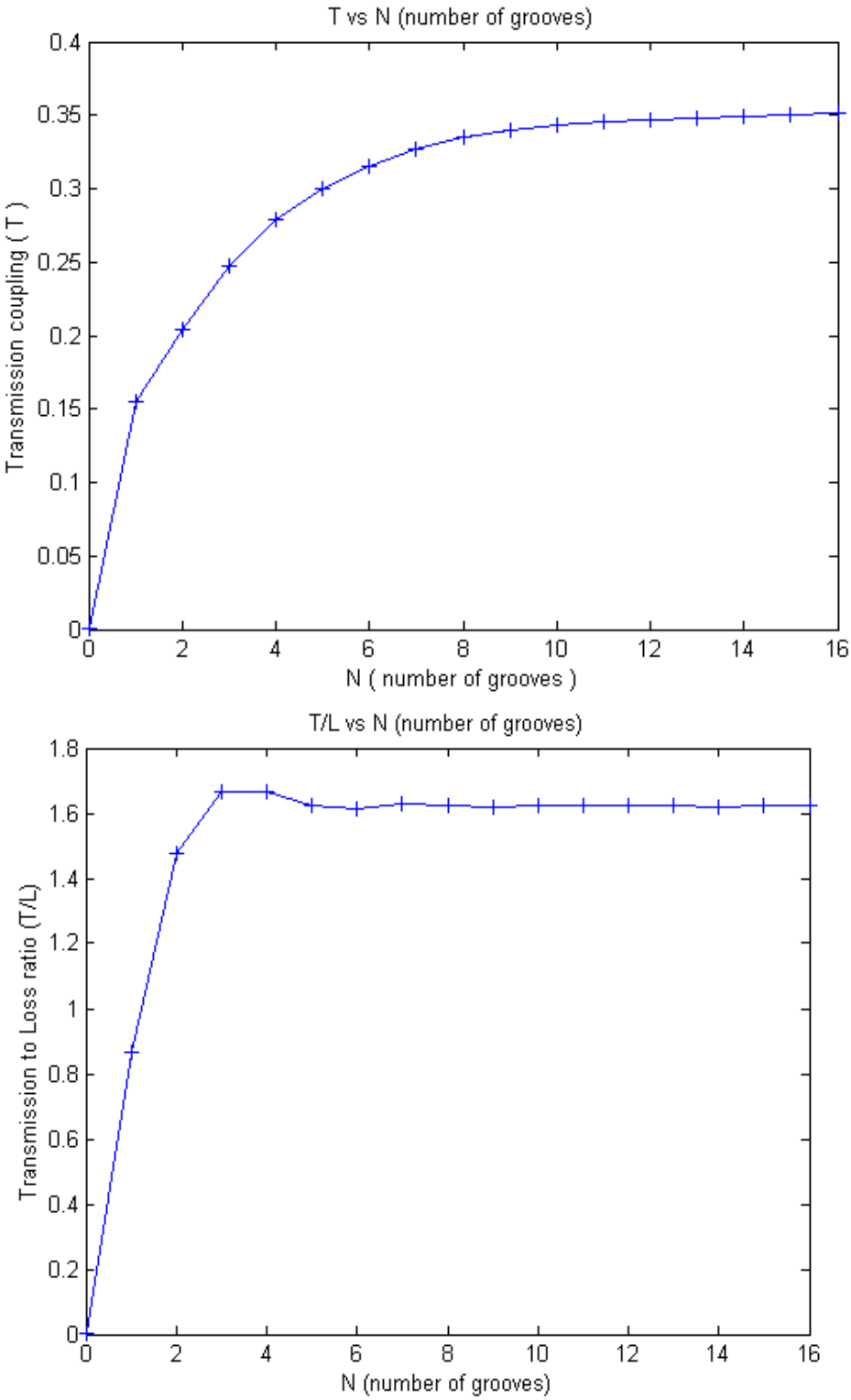

Figure 5.1. (Top) Optimum transmission coupling factor T, (bottom) optimum transmission to loss ratio T/L, as functions of the number of grooves N.

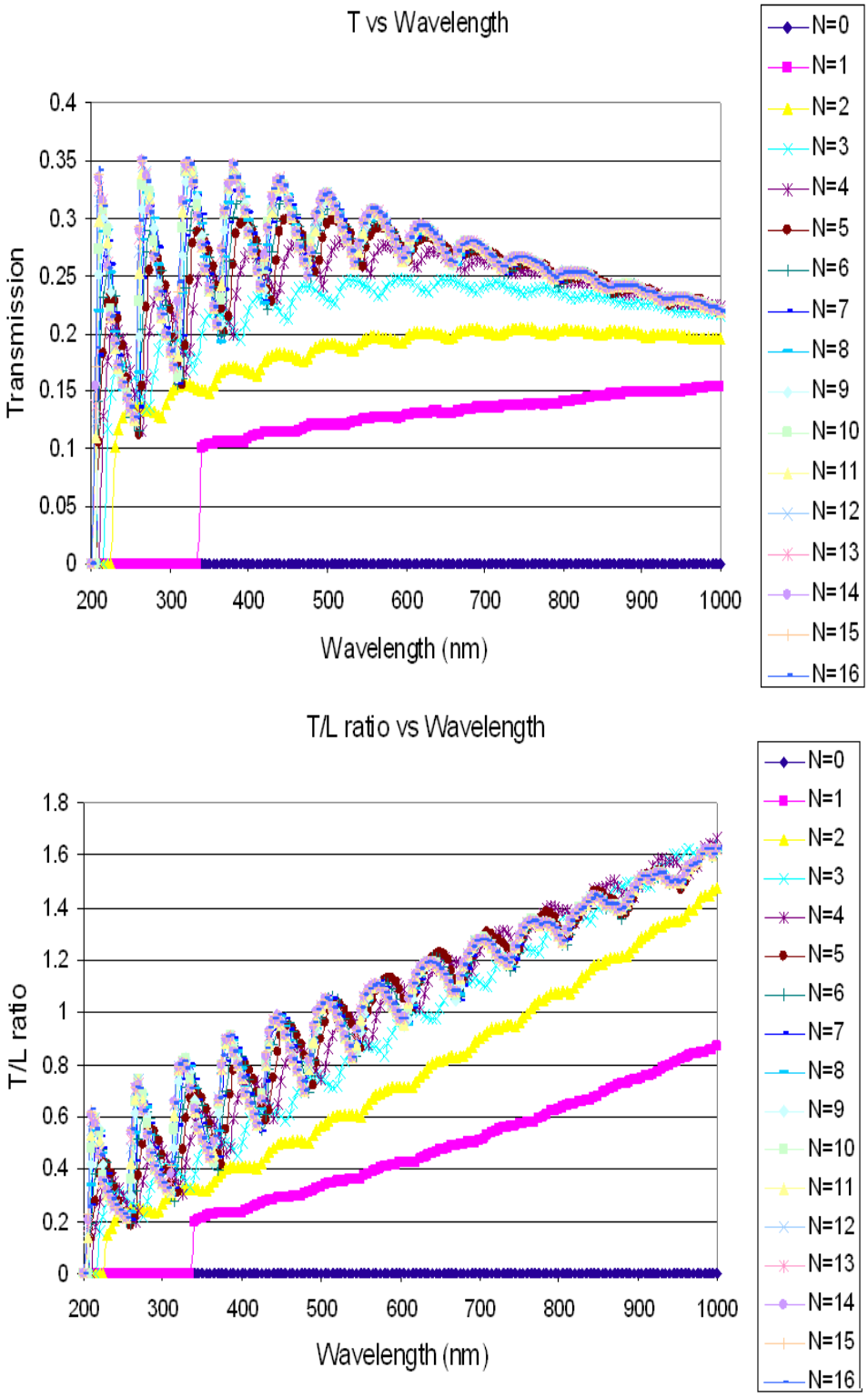

Figure 5.2. (Top) Optimum transmission coupling factor T, (bottom) optimum transmission to loss ratio T/L, as functions of the number of grooves N and wavelength λ.

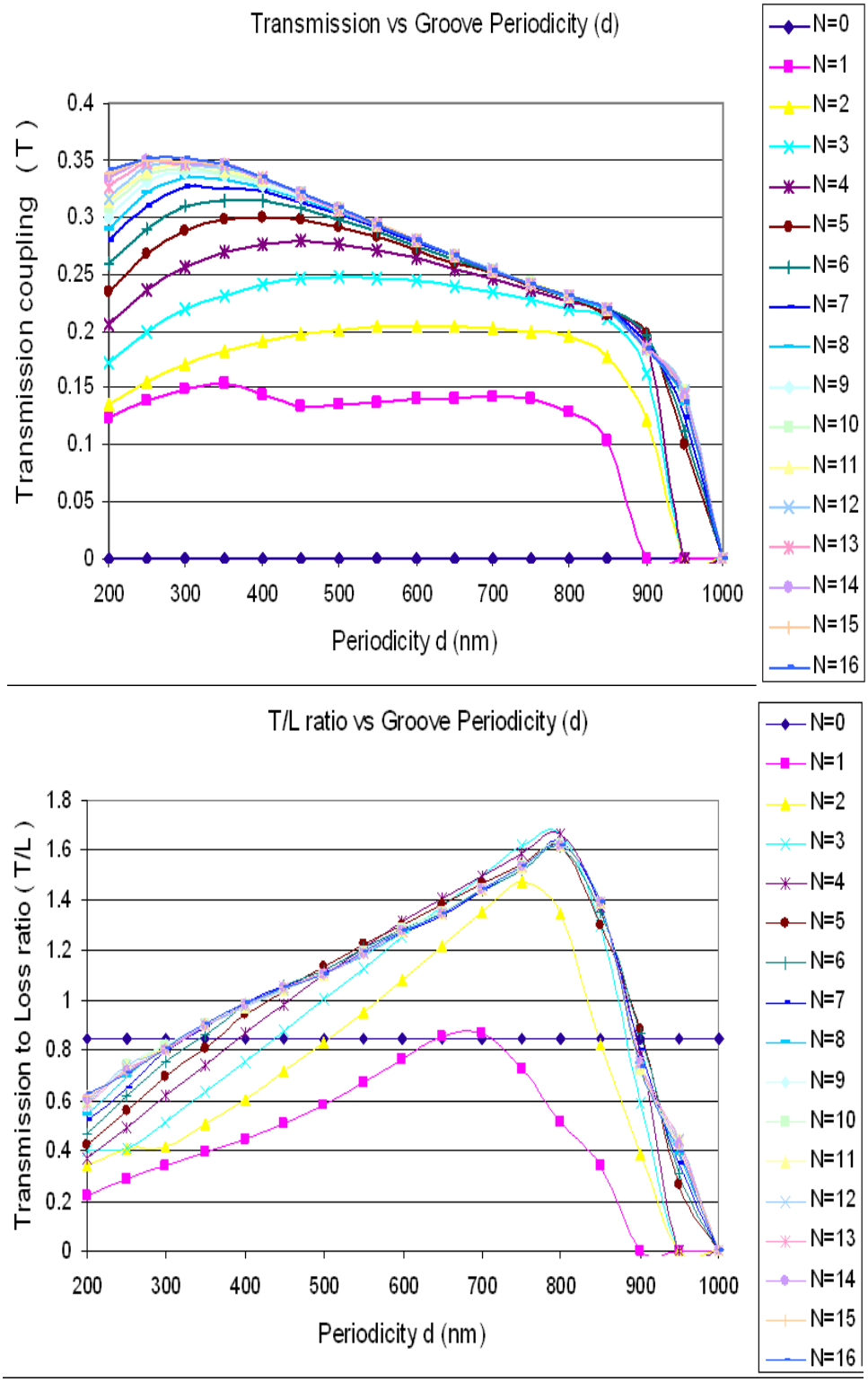

Figure 5.3. (Top) Optimum transmission coupling factor T, (bottom) optimum transmission to loss ratio T/L, as functions of the number of grooves N and groove period d.

Table 5.1. Peak values of transmission coupling T to TEM0 Gaussian mode, at the optimum combination of number of grooves N, wavelength λ, groove period d, groove depth h, and Gaussian-mode focus position z_0, with waist set at $a_0 = 1.4$ μm.

Maximized transmission coupling T							
N	λ (nm)	d (nm)	h (nm)	T	T/L	T_{total}	z_0 (nm)
0	200	200	10.1	0.00058	0.84326	0.000696	-4.41786
1	1000	350	218.1	0.155	0.55973	0.382	307.876
2	745	600	148.1	0.205	0.43228	0.898	0
3	590	500	110.1	0.247	0.53667	0.853	1043.65
4	515	450	90.1	0.279	0.58595	0.909	2391.27
5	450	400	74.1	0.3	0.63006	0.908	4105.01
6	445	400	72.1	0.315	0.6464	0.948	6918.56
7	330	300	48.1	0.327	0.74146	0.788	7463.66
8	330	300	48.1	0.335	0.74426	0.82	11195.5
9	325	300	46.1	0.34	0.7788	0.774	11367.7
10	325	300	46.1	0.344	0.78025	0.787	16104.3
11	325	300	46.1	0.346	0.783	0.791	19893.5
12	325	300	46.1	0.347	0.78567	0.79	23682.8
13	265	250	32.1	0.348	0.83936	0.708	22074.1
14	265	250	32.1	0.349	0.84024	0.711	27883.1
15	265	250	32.1	0.35	0.84189	0.712	33692.1
16	265	250	32.1	0.351	0.84382	0.713	39501.1

size of Gaussian mode is constant for all λ, but the beam waist is proportional to λ, we have performed another optimization run presented in Section 5.2.

5.2 Optimization of T and T/L metrics with a scaled beam waist

In this run of simulations, we choose $a_0 = 1.4$ μm at $\lambda = 560$ nm and scale a_0 proportionally to λ for all other wavelengths, i.e. $a_0(\lambda) = 1.4$ μm $\times$ $\lambda/(560$ nm).

The peak transmission of $T = 0.407$ takes place for depth $h = 30.1$ nm, number of grooves $N = 14$, period $d = 200$ nm, slit width $a = 40$ nm, wavelength $\lambda = 225$ nm, and $z_0 = 9056.62$ nm. For this geometry, $T/L = 1.036$.

Table 5.2. Peak values of transmission coupling to loss ratio T/L for TEM0 Gaussian mode, at the optimum combination of number of grooves N, wavelength λ, groove period d, groove depth h, and Gaussian-mode focus position z_0, with waist set at $a_0 = 1.4$ μm.

Maximized transmission to loss ratio T/L							
N	λ (nm)	d (nm)	h (nm)	T/L	T	T_{total}	z_0 (nm)
0	200	200	10.1	0.84326	0.00058	0.000696	-4.41786
1	1000	700	212.1	0.868	0.140276	0.30185	0
2	1000	750	210.1	1.48	0.191541	0.3212	923.628
3	1000	800	206.1	1.66	0.213802	0.34223	3386.64
4	1000	800	206.1	1.67	0.22066	0.35318	6773.27
5	990	800	204.1	1.62	0.222854	0.36033	8085.63
6	1000	800	206.1	1.61	0.214094	0.34692	7696.9
7	1000	800	206.1	1.63	0.216476	0.34927	7696.9
8	985	800	202.1	1.62	0.223162	0.36052	9064.37
9	1000	800	206.1	1.62	0.215276	0.34823	7696.9
10	1000	800	206.1	1.62	0.2157	0.34868	7696.9
11	985	800	202.1	1.62	0.222665	0.36	9064.37
12	1000	800	206.1	1.62	0.215546	0.34849	7696.9
13	1000	800	206.1	1.62	0.215587	0.34853	7696.9
14	1000	800	206.1	1.62	0.215525	0.34849	7696.9
15	1000	800	206.1	1.62	0.215574	0.34852	7696.9
16	1000	800	206.1	1.62	0.215544	0.3485	7696.9

The peak $T/L = 1.134$ occurs for $h = 164.1$ nm, $N = 13$, $d = 750$ nm, $a = 40$ nm, $\lambda = 850$ nm, and $z_0 = 30876$ nm. For that geometry, $T = 0.239$.

The optimum values of T and T/L for scaled a_0 are shown in Tables 5.3 and 5.4. The global peak T and T/L values are plotted as functions of the number of corrugations N in Fig. 5.4. Graphs showing optimum T and T/L values as functions of wavelength λ and groove period d are reported in Figs. 5.5 and 5.6, respectively. A saturation in T/L values at longer wavelengths, or longer groove periods, is seen from Figs. 5.5 and 5.6. The fact that T/L stabilises at longer wavelengths is more relevant to the practical situation, as was explained in the previous Section 5.1. This concludes our results for this thesis.

Table 5.3. Peak values of transmission coupling T to TEM0 Gaussian mode, at the optimum combination of number of grooves N, wavelength λ, groove period d, groove depth h, and Gaussian-mode focus position z_0, with a scaled beam waist.

Maximized transmission coupling T							
N	λ (nm)	d (nm)	h (nm)	T	T/L	T_{total}	z_0 (nm)
0	200	200	10.1	0.0646	0.083	0.84326	0
1	280	200	50.1	0.179	0.3768	0.65325	0
2	250	200	40.1	0.277	0.6385	0.71049	0
3	240	200	36.1	0.341	0.8622	0.73555	706.858
4	235	200	34.1	0.376	0.9916	0.75492	1614.97
5	230	200	32.1	0.394	1.04	0.77363	2709.62
6	230	200	32.1	0.4	1.046	0.78314	4290.24
7	225	200	30.1	0.402	1.009	0.79992	5522.33
8	225	200	30.1	0.404	1.012	0.80397	7510.37
9	225	200	30.1	0.405	1.02	0.8027	8393.94
10	225	200	30.1	0.405	1.025	0.79953	8614.84
11	225	200	30.1	0.405	1.029	0.79794	8614.84
12	225	200	30.1	0.406	1.032	0.79842	8614.84
13	225	200	30.1	0.407	1.035	0.7996	8835.73
14	225	200	30.1	0.407	1.036	0.80011	9056.62
15	225	200	30.1	0.407	1.034	0.79983	9056.62
16	225	200	30.1	0.406	1.033	0.79943	8835.73

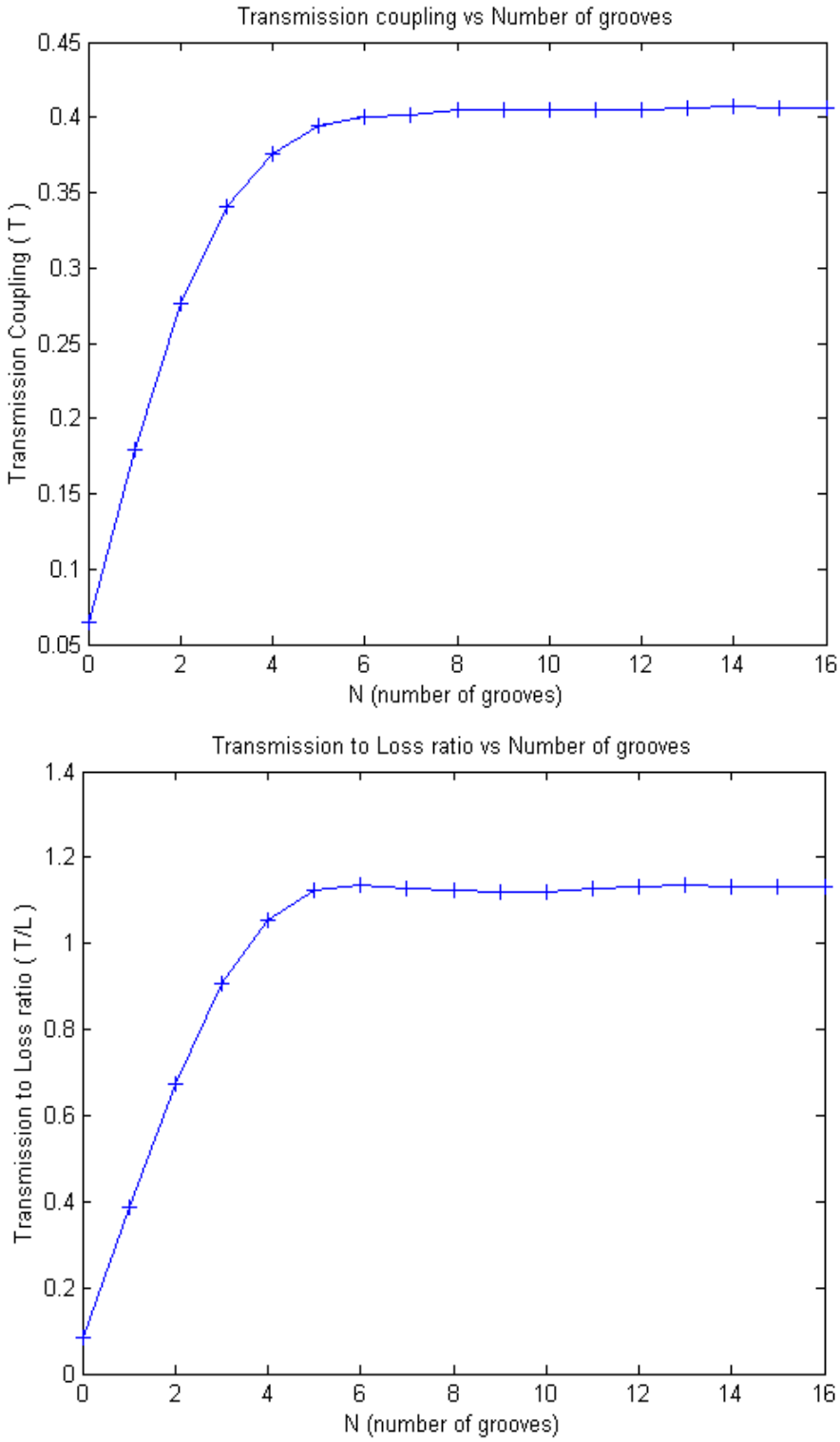

Figure 5.4. Scaled waist case, (top) optimum transmission coupling factor T, (bottom) optimum transmission to loss ratio T/L, as functions of the number of grooves N.

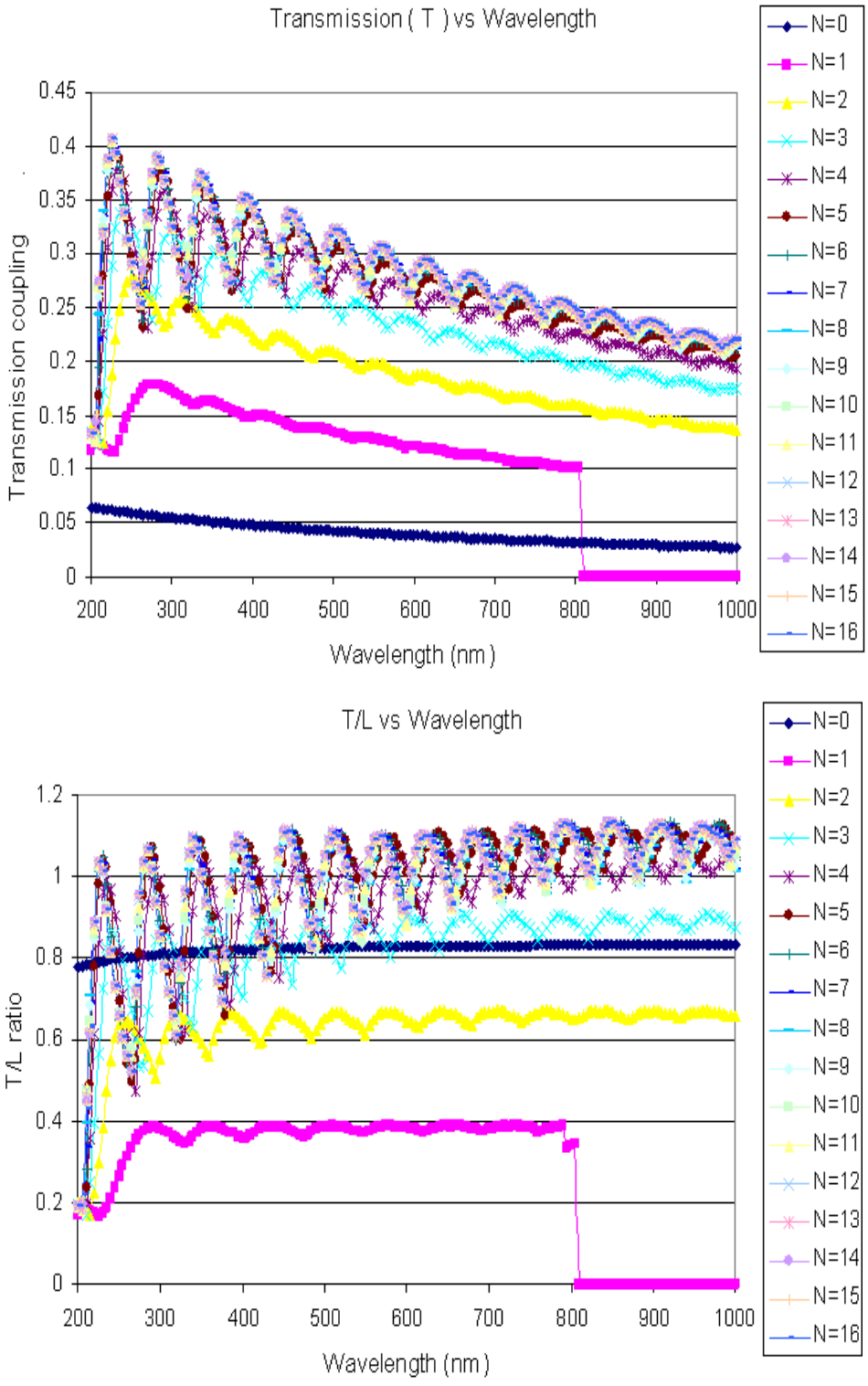

Figure 5.5. Scaled waist case, (top) optimum transmission coupling factor T, (bottom) optimum transmission to loss ratio T/L, as functions of the number of grooves N and wavelength λ.

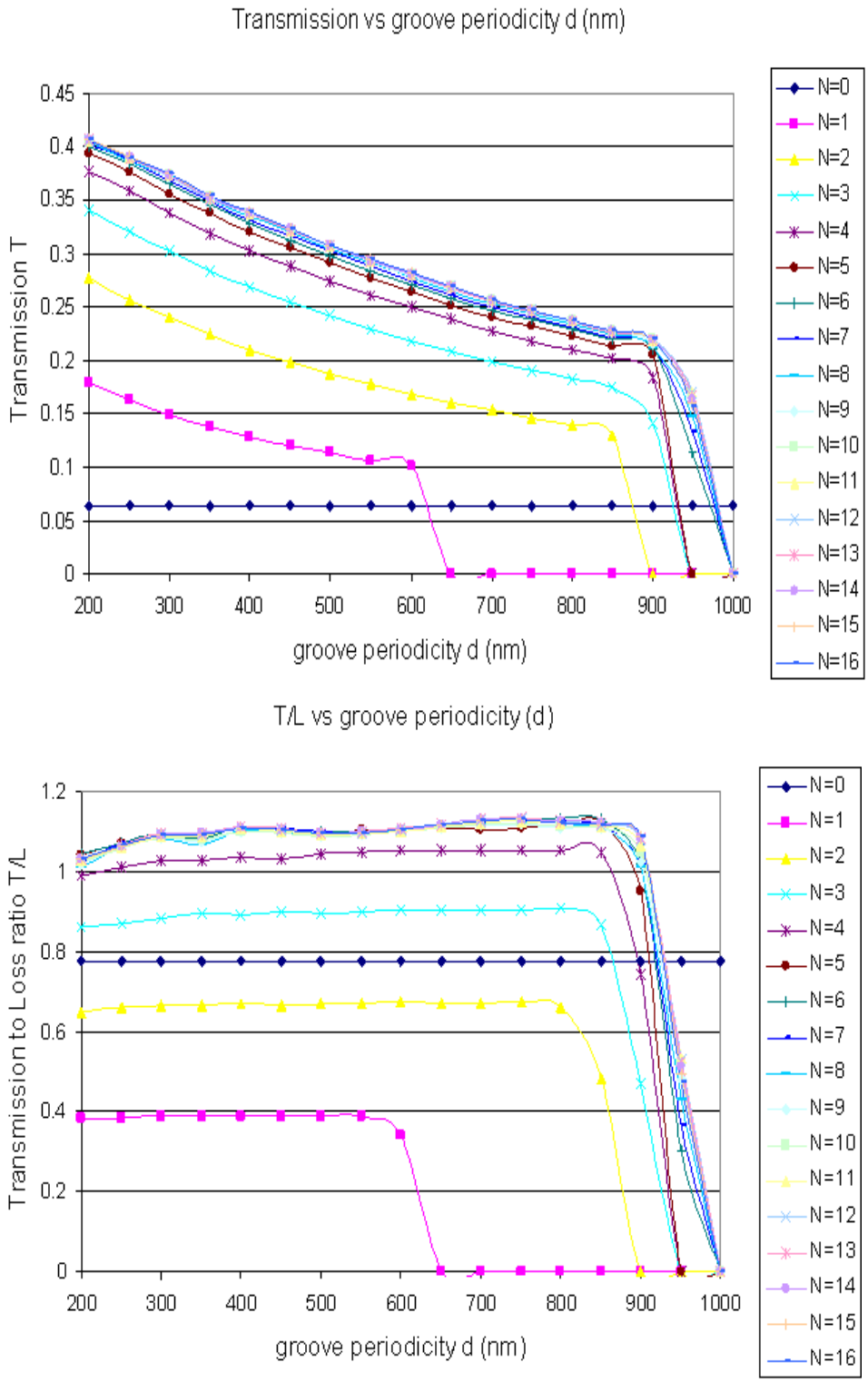

Figure 5.6. Scaled waist case, (top) optimum transmission coupling factor T, (bottom) optimum transmission to loss ratio T/L, as functions of the number of grooves N and groove period d.

Table 5.4. Peak values of transmission coupling to loss ratio T/L for TEM0 Gaussian mode, at the optimum combination of number of grooves N, wavelength λ, groove period d, groove depth h, and Gaussian-mode focus position z_0, with a scaled beam waist.

Maximized transmission to loss ratio T/L							
N	λ (nm)	d (nm)	h (nm)	T/L	T	T_{total}	z_0 (nm)
0	200	200	10.1	0.083	0.0646	0.84326	0
1	730	500	150.1	0.3884	0.105	0.37436	0
2	960	750	198.1	0.6731	0.136	0.33794	942.478
3	965	800	196.1	0.9077	0.173	0.36314	2842.16
4	945	800	190.1	1.056	0.197	0.38373	6494.26
5	985	850	198.1	1.122	0.205	0.38841	11604.3
6	920	800	182.1	1.134	0.222	0.41696	17160.9
7	855	750	166.1	1.127	0.237	0.44732	21824.3
8	855	750	166.1	1.122	0.238	0.44937	26021.2
9	850	750	164.1	1.119	0.239	0.45263	29207
10	850	750	164.1	1.121	0.238	0.44963	30041.5
11	850	750	164.1	1.127	0.237	0.44828	30041.5
12	850	750	164.1	1.132	0.238	0.4489	30041.5
13	850	750	164.1	1.134	0.239	0.44994	30876
14	850	750	164.1	1.133	0.239	0.45022	30876
15	850	750	164.1	1.131	0.239	0.44988	30876
16	850	750	164.1	1.131	0.239	0.4496	30876

CHAPTER 6

CONCLUSION

In this thesis we have shown theoretically the method to optimize the transmission coupling to a Gaussian mode from a 1D sub-wavelength metal nanoaperture surrounded by periodic corrugations. We have characterized the effect of various parameters on the transmission coupling factor T and transmission coupling to loss ratio T/L. We have optimized the values of the parameters of metal nanostructure, such as number of corrugations, groove depth, and groove periodicity, to find maximum T and T/L for a given wavelength.

We have achieved optimum $T = 0.35$ and $T/L = 1.67$ for a Gaussian beam with waist size $a_0 = 1.4$ μm independent of the wavelength, as well as $T = 0.4$ and $T/L = 1.13$ for that with beam waist size linearly proportional to the wavelength.

The future work is to use these results to realize a single-photon source with high coupling efficiency to an optical fiber.

APPENDIX A

SURFACE PLASMONS

A.1 OVERVIEW OF SURFACE PLASMONS

The surface plasmons are bound waves created at the metal-dielectric interface, when excited by TM-polarized light. They exist as bound waves because of a momentum mismatch at the boundary with respect to the corresponding wave propagating in air.

We will start by considering Drude model of metal conductivity [13]. Drude model yields metal permittivity

$$\epsilon = \epsilon_1 - i\frac{\varepsilon}{\omega\epsilon_0} \ , \tag{A.1}$$

where ϵ_1 represents the contribution of bound electrons, and

$$\sigma = \frac{\sigma_0}{1 + i\omega/\nu} \ , \tag{A.2}$$

with ν being the frequency of collisions between the electrons and the lattice, and $\sigma_0 = n_e e^2/(m\nu)$ being the DC value of the conductivity (n_e—concentration of the electrons, whereas e and m are electronic charge and mass, respectively). Collision frequency ν is related to electron mobility $\mu = e/(m\nu)$. Thus, Equation (A.1) can be rewritten as

$$\begin{aligned} \epsilon &= \epsilon_1 - \frac{n_e e^2}{m\epsilon_0(\nu^2+\omega^2)} - i\frac{n_e e^2 \nu}{m\epsilon_0\omega(\nu^2+\omega^2)} \\ &= \epsilon' - i\epsilon'' = (n - i\kappa)^2, \end{aligned} \tag{A.3}$$

$$\epsilon' = n^2 - \kappa^2, \tag{A.4}$$

$$\epsilon'' = 2n\kappa^2. \tag{A.5}$$

For typical metals, we have $\epsilon' < 0$.

The nature of the plasmonic waves is such that the electric fields decay along the direction of propagation in the surface as $e^{-\alpha z/2}$, where the attenuation constant is given

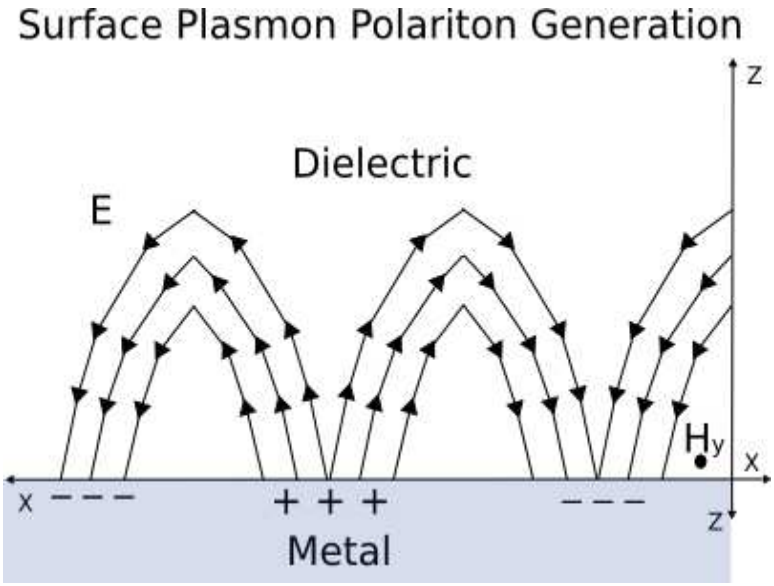

Figure A.1. A schematic of the surface plasmon generation in metal-dielectric interface .

by $\alpha \approx 4\pi n/(\kappa^3\lambda)$ for $n \ll \kappa$, typical for good conductors. In contrast to that, a conventional electromagnetic wave propagating into the absorbing medium with $\kappa \ll n$ is attenuated with $\alpha = 4\pi\kappa/\lambda$.

The plasmon has a propagation constant given by

$$\beta = \sqrt{\frac{\epsilon_d \epsilon'}{\epsilon_d + \epsilon'}} \frac{\omega}{c} \ , \tag{A.6}$$

where ϵ_d is the permittivity of the dielectric above the metal surface. Plasmon attenuation factor is

$$\alpha = \frac{\epsilon_d^{3/2} \epsilon''}{\sqrt{\epsilon' \left(\epsilon_d + \epsilon'\right)^3}} \frac{\omega}{c} \ , \tag{A.7}$$

and the plasmon resonance takes place at $\epsilon_d = -\epsilon'$.

Now, we can consider several limiting cases.

- *Free-electron plasma*:

  If $\nu = 0$ (no collisions), we have $\sigma = -in_e e^2/(m\omega)$, and

$$\epsilon = \epsilon' = \epsilon_1 - \frac{n_e e^2}{m\epsilon_0 \omega^2} = \epsilon_1 - \left(\frac{\omega_p}{\omega}\right)^2, \tag{A.8}$$

  where $\omega_p = \sqrt{n_e e^2/(m\epsilon_0)}$ is the plasmon frequency. In free-electron plasma, $\epsilon_1 = 1$ and

$$\epsilon = 1 - \left(\frac{\omega_p}{\omega}\right)^2. \tag{A.9}$$

  For $\omega < \omega_p$, $\epsilon = \epsilon' < 0$, therefore we have limited $1/e$ field penetration depth δ into the metal. For $\omega \ll \omega_p$, we have an almost *perfect conductor*, where $\delta \approx \sqrt{m/(\mu_0 n_e e^2)} = c/\omega_p$ is small.

  Free-electron plasma is a good approximation for pure crystal metals at low temperatures, as well as for superconductors at near-zero temperatures and $\hbar\omega < \Delta$ (where Δ is the energy gap in electron fluid spectrum).

  Note that for vacuum-plasma interface, the plasmonic resonance takes place at $\epsilon = -1$, i.e. at $\omega = \omega_p/\sqrt{2}$.

- *Low frequency (DC and RF) case*:

  If $\nu \neq 0$, but $\sigma_0 \gg \omega\epsilon_1\epsilon_0$, i.e $\omega \ll \omega_p^2/(\epsilon_1\nu)$, as well as $\omega \ll \nu$, then

$$\epsilon \approx -i\frac{\sigma_0}{\omega\epsilon_0}\ . \tag{A.10}$$

  This, again, means exponential attenuation of the wave over skin depth $\delta = \sqrt{\frac{2}{\omega\mu_0\sigma_0}} = \frac{c}{\omega_p}\sqrt{\frac{2\nu}{\omega}}$. Such material is referred to as *good conductor*. Please note

that penetration depth in this case is $\sqrt{\frac{2\nu}{\omega}}$ times greater than that for free-electron plasma, i.e plasma is a better conductor than a *good conductor*.

REFERENCES

[1] L. Martin-Moreno, F. J. Garcia-Vidal, H. J. Lezec, A. Degiron, and T. W. Ebbesen, "Theory of highly directional emission from a single subwavelength aperture surrounded by surface corrugations," Phys. Rev. Lett. **90**, 167401 (2003).

[2] M. Vasilyev and P. Kumar, "Efficient coupling between Gaussian cavity mode and metal nanoaperture," NanoPhotonics in Information Sciences conference, San Diego, CA, April 2005, paper NWB4.

[3] H. J. Lezec, A. Degiron, E. Devaux, R. A. Linke, L. Martin-Moreno, F. J. Garcia-Vidal, and T. W. Ebbesen, "Beaming light from a subwavelength aperture," Science **297**, 820 (2002).

[4] F. J. Garcia-Vidal, H. J. Lezec, T. W. Ebbesen, and L. Martin-Moreno, "Multiple paths to enhance optical transmissions through a single subwavelength slit," Phys. Rev. Lett. **90**, 213901 (2003).

[5] W. L. Barnes, A. Dereux, and T. W. Ebbesen, "Surface plasmon subwavelength optics," Nature **424**, 824 (2003).

[6] J. Bravo-Abad, F. J. Garcia Vidal, and L. Martin-Moreno, "Resonant Transmission of Light Through Finite Chains of Subwavelength Holes in a Metallic Film," Phys. Rev. Lett. **93**, 227401 (2004).

[7] F. J. Garcia-Vidal, L. Martin-Moreno, H. J. Lezec, and T. W. Ebbesen, "Focusing light with a single-subwavelength aperture flanked by surface corrugations," Appl. Phys. **83**, 4500 (2003).

[8] J. B. Pendry, L. Martin-Moreno, and F. J. Garcia-Vidal, "Mimicking Surface Plasmons with Structured Surfaces," Science **305**, 847 (2004).

[9] E. M. Purcell, "Spontaneous emisssion probabilities at radio frequencies," Phys. Rev. Lett. **69**, 681 (1946).

[10] M. Pelton, C. Santori, J. Vuckovic, B. Zhang, G. S. Solomon, J. Plant, and Y. Yamamoto, "Efficient source of single photons: a single quantum dot in a micropost microcavity," Phys. Rev. Lett. **86**, 233602 (2002).

[11] M. Vasilyev, "*Reduced forms of nanoaperture field integrals*," personal communication, 2006.

[12] M. Born and E. Wolf, "*Principles of Optics*," 7th ed., Cambridge University Press, 1999.

[13] S. Ramo, J. R. Whinnery, and T. Van Duzer, "*Fields and waves in communication*," 2nd ed., John Wiley & Sons, NewYork, 1984.

[14] J. W. Goodman, "*Introduction to Fourier Optics*," 2nd ed., McGraw-Hill, 1996.

BIOGRAPHICAL STATEMENT

Muthiah Annamalai got his B.Tech in Electronics and Communication Engineering in 2005 from National Institute of Technology-Tirchy, India. He is curious about science, and professionally interested in Nonlinear Optics, Quantum Optics, and Quantum Information Processing. Muthiah likes outdoor activities.